Current Stress Optimization of Dual Active Bridge Converter in Two-Stage Single-Phase Inverter System With Second Harmonic Current Shaping

Fei Xiong, Junchi Li, Dong Yan, and Xiaolei Chen

***Abstract*—With consideration of double line-frequency instantaneous power in two-stage single-phase inverter system, a second harmonic current shaping (SHCS) method is proposed in this article to minimize the current stress of front-end dual active bridge (DAB) dc/dc converter. The current stress of DAB is optimized by analytical expressions in time domain so that both the low-frequency fluctuations and inherent high-frequency characteristics of DAB current are considered. As a result, the current stress of DAB can be minimized. The analytical expressions of optimized double line-frequency output current of DAB are derived. An implementation method is presented to combine the traditional single voltage closed-loop (SVC) control method with the feedforward compensation of only double line-frequency output current of DAB. Therefore, the stability and dynamic performance of SVC are not affected by SHCS method. The parameters design of SHCS method is the same as that of SVC method. The minimum current stress and fast dynamic response can be achieved by SHCS method without any compromise. The performance evaluation indicates that SHCS method is superior to traditional methods in terms of optimization effects and implementation method. The experimental results verify the good performance of SHCS method both in steady state and dynamic state.**

***Index Terms*—Current stress, double line-frequency, dual active bridge (DAB), power electronics transformer (PET).**

I. INTRODUCTION

POWER electronics transformer (PET) provides galvanic isolation by means of medium-frequency transformers instead of conventional line-frequency transformer. Many topologies of PET have been proposed in different applications [1]. The PET consists of dual active bridge (DAB) dc/dc converter and H-bridge dc/ac converter is one of the most widely studied topology [2]. The two-stage single-phase inverter system, consisting of front-end DAB converter and downstream H-bridge converter, is the elementary unit of this PET, as shown in Fig. 1.

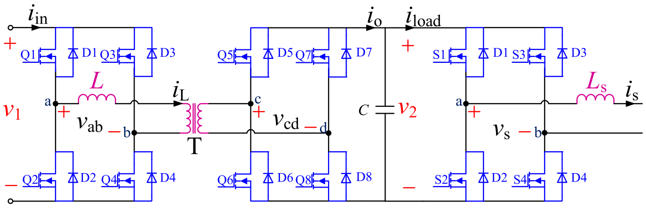

Fig. 1. DAB dc–dc converter driving an H-bridge single-phase inverter.

The two-stage inverter system or PET has wide application prospects in railway traction, MV distribution grid, renewable energy integration, energy storage, etc. [3]–[6].

The instantaneous power in a single-phase inverter system will fluctuate at double line-frequency. This fluctuating power will induce the unwanted low-frequency fluctuations both in dc-bus voltage and the current in front-end dc/dc converter.

The third harmonic injection method is used to reduce the double line-frequency power in downstream single-phase H-bridge converter and improve the utility ratio of dc voltage. By this way, both the low-frequency fluctuations in dc voltage and current can be reduced. In [7], third harmonic voltage is injected to cascaded H-bridge (CHB) to minimize dc voltage and reduce switching losses. In [8], third harmonic voltage is injected to CHB to extend the operation ranges under power imbalance conditions and reduce the dc-link voltage fluctuation. In [9], third harmonic voltage is injected to CHB to minimize the current stress in series-resonant DAB converter. However, the capacity of third harmonic injection method to reduce double line-frequency power in ac side is limited by maximum modulation index of CHB. As a result, the reduction of low-frequency fluctuations in system by third harmonic injection may be small.

Many studies focus on eliminating the low-frequency fluctuations in dc-bus voltage. In [10] and [11], an additional active filter is equipped to supply the low-frequency fluctuating power so that the front-end dc/dc converter only provides the dc power. However, the additional converter adds the cost, losses, weight, and size to the system. To avoid adding extra devices, some studies utilize the front-end dc/dc converter to transfer the low-frequency power from one dc side to the other, so that the low-frequency fluctuations in intermediate dc-bus voltage can be eliminated. In [12] and [13], the proportion integration resonance controller is used in the closed-loop control system. In [14], the traditional proportional–integral (PI) controller is

---

Manuscript received February 15, 2021; revised July 6, 2021; accepted August 18, 2021. Date of publication September 3, 2021; date of current version November 30, 2021. This work was supported by the Science and Technology Research Program of Chongqing Municipal Education Commission under Grant KJQN202000620. Recommended for publication by Associate Editor A. Yazdani. (*Corresponding author: Fei Xiong.*)

Fei Xiong, Dong Yan, and Xiaolei Chen are with the College of Automation, Chongqing University of Posts and Telecommunications, Chongqing 400065, China (e-mail: xiongfei@cqupt.edu.cn; yandong@cqupt.edu.cn; chenxiaolei@cqupt.edu.cn).

Junchi Li is with the School of Electrical Engineering, Beijing Jiaotong University, Beijing 100044, China (e-mail: 18810589285@163.com).

Color versions of one or more figures in this article are available at https://doi.org/10.1109/TPEL.2021.3110110.

Digital Object Identifier 10.1109/TPEL.2021.3110110

combined with second-order filter to control the fluctuating power of DAB. In [15], the low-frequency fluctuating power in intermediate dc-bus is supplied totally by front-end DAB converter with the help of nonlinear disturbance observer. However, the low-frequency fluctuating power which is totally supplied by front-end dc/dc converter will induce violent fluctuations in the current of front-end converter, leading to not only higher current stress in the power switches but also larger power losses in the converter.

A large number of literatures discuss the modulation methods to minimize the current stress or current root-mean-square (rms) of DAB just in one switching period [16]–[18] but without considering the double line-frequency fluctuations. Different from these literatures, some other literatures focus on suppressing the low-frequency fluctuations in the input/output current of front-end dc/dc converter caused by double line-frequency power. The simplest way to suppress the low-frequency current fluctuations is to cut down the closed-loop bandwidth of front-end dc/dc converter by reducing control parameters or adding low-pass filter [19], [20]. However, the system will suffer poor dynamic performance due to low bandwidth. To solve this problem, the second-order filter is incorporated into the closed-loop system to reduce only the double line-frequency components in the system, so that the dynamic performance can be improved [21]–[23]. However, the notch filter will bring about negative phase-shift in the system and the band-pass filter will bring about a phase rotation of π, which limits the bandwidth of the system. Moreover, the parameter design of the control system with second-order filters is sophisticated. Poor design of the control parameters and filter parameters may lead to instability [24].

There are few pieces of literature investigating the method to suppress the low-frequency current fluctuations especially in DAB. These methods [19]–[23] are generally designed for traditional buck/boost derived converter in frequency domain. In these converters, the high-frequency components in input or output current have been attenuated significantly by large filter inductance. Therefore, these methods have no need to consider the high-frequency components in current. By contrast, the current in DAB contains considerable high-frequency components at switching frequency (leakage inductance current) or at twice the switching frequency (input/output current), as shown in Fig. 2. No filter inductances are placed in the input/output dc side of DAB. The current stress of DAB is affected by both low-frequency fluctuations and inherent high-frequency characteristics. As a result, the current stress of DAB still cannot be minimized, even if the low-frequency fluctuations in the input or output current of DAB have been eliminated.

In this article, a second harmonic current shaping (SHCS) method is proposed to minimize the current stress of DAB in consideration of low-frequency fluctuations caused by double line-frequency power. Unlike the traditional methods [19]–[23] in frequency domain, the proposed method is in the view of time domain. First, the propagation paths of low-frequency fluctuations in DAB two-stage single-phase inverter system are analyzed. The analytical expressions in time domain of current stress are derived in consideration of both the low-frequency fluctuations and inherent high-frequency characteristics of DAB. Then, the double line-frequency component in the output current of DAB is optimized for the purpose of minimizing the current stress of DAB under different dc voltage and power factor. The analytical expressions of optimized second-harmonic output current are derived with some approximations and simplifications. An implementation method is presented to shape the double line-frequency output current of DAB by feedforward compensation. Next, the performance evaluation of SHCS method is provided. The optimization effects and implementation method of SHCS method are compared to traditional methods. Finally, the experimental results by a downscaled prototype verify the good optimization effects of SHCS method.

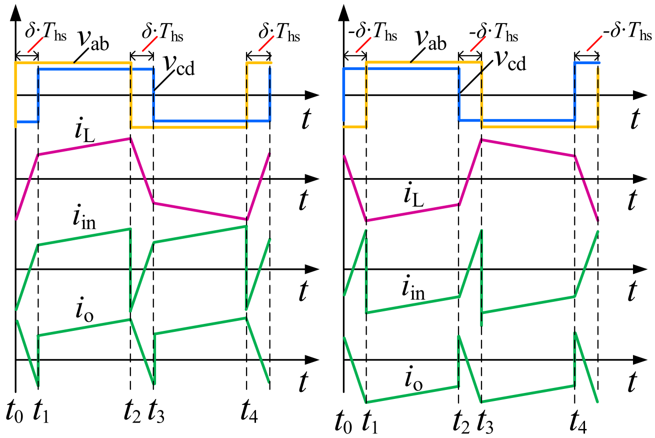

(a) (b)

Fig. 2. Waveforms of DAB current under SPS control. (a) $\delta \geq 0$. (b) $\delta < 0$.

The rest of this article is organized as follows. In Section II, operational principles of the DAB are introduced and the propagation paths of low-frequency fluctuations are analyzed. In Section III , the analytical expressions of current stress are derived. In Section IV, the second-harmonic output current of DAB is optimized. In Section V, performance of proposed SHCS method is evaluated. In Section VI, the feasibility and effectiveness of proposed SHCS method are verified by experimental results. Finally, Section VII concludes this article.

II. TWO-STAGE SINGLE-PHASE INVERTER SYSTEM

A. Topology

The two-stage single-phase inverter system is shown in Fig. 1. The inductance L which is reflected to the primary side denotes the equivalent leakage inductance of transformer T. The capacitance in intermediate dc-bus is C. v_1 and v_2 are the dc-bus voltage in primary side (input side) and secondary side (output side), respectively. The current through the leakage inductance L is i_L. The output current i_o of DAB and the load current i_{load} are also marked in Fig. 1. The turns ratio n of transformer T is set to 1, so that the analysis can be simplified. When $n \neq 1$, the analysis method is similar to the situation when $n = 1$. v_{s} and i_{s} are the output voltage and current of H-bridge, respectively. The reference positive direction of voltages and currents has been marked in Fig. 1.

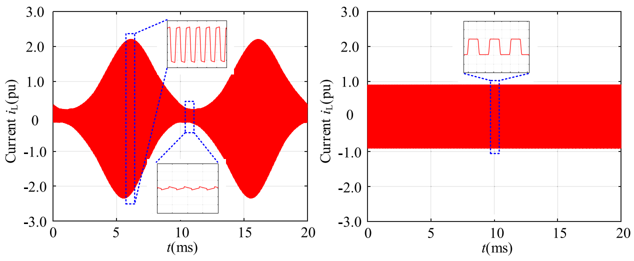

(a) (b)

Fig. 3. DAB leakage current i_L under (a) single-phase ac load and (b) dc load.

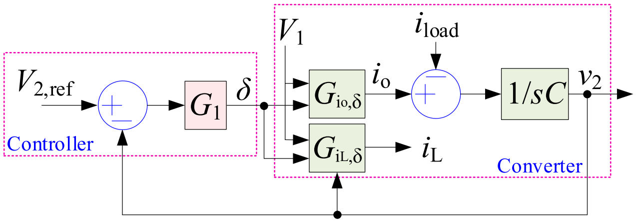

Fig. 4. Single voltage closed-loop (SVC) control of DAB.

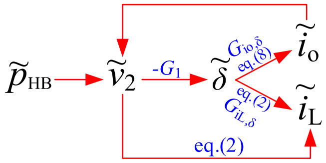

Fig. 5. Propagation of low-frequency fluctuations in DAB.

B. Single-Phase-Shift (SPS) Operating Principle

Single phase shift (SPS) is the simplest and most widely used modulation strategy of DAB. The working waveforms of DAB converter under SPS are shown in Fig. 2. T_s is the switching period of DAB. $\delta \cdot T_{\mathrm{hs}}$ is the phase-shift time between v_{ab} and v_{cd}, where T_{hs} is the half switching period of DAB and δ is the phase-shift ratio between v_{ab} and v_{cd}.

The average output power of DAB during a switching period is

$$p_{\mathrm{DAB}} = i_o v_2 = \frac{v_1 v_2 \delta(1-|\delta|)T_{\mathrm{hs}}}{L} \tag{1}$$

where i_o is the average output current during a switching period of DAB. v_1 and v_2 are the average dc voltage during a switching period of DAB. The switching frequency of DAB is generally much larger than line-frequency 50 Hz, so i_o can be solved by using (1) regardless of the high-frequency components.

Under steady-state conditions, the values of leakage inductance current at specific switching moments are

when δ

$$\geq 0, \begin{cases} i_{\mathrm{L}}(t_0) = i_{\mathrm{L}}(t_4) = -i_{\mathrm{L}}(t_2) = \frac{(v_2-v_1)T_{\mathrm{hs}}-2v_2\delta T_{\mathrm{hs}}}{2L} \\ i_{\mathrm{L}}(t_1) = -i_{\mathrm{L}}(t_3) = \frac{(v_2-v_1)T_{\mathrm{hs}}+2v_1\delta T_{\mathrm{hs}}}{2L} \end{cases}$$

when δ

$$< 0, \begin{cases} i_{\mathrm{L}}(t_0) = i_{\mathrm{L}}(t_4) = -i_L(t_2) = \frac{(v_2-v_1)T_{\mathrm{hs}}+2v_1(-\delta)T_{\mathrm{hs}}}{2L} \\ i_{\mathrm{L}}(t_1) = -i_{\mathrm{L}}(t_3) = \frac{(v_2-v_1)T_{\mathrm{hs}}-2v_2(-\delta)T_{\mathrm{hs}}}{2L}. \end{cases} \tag{2}$$

C. Propagation of Low-Frequency Fluctuations in DAB

There is significant double line-frequency power fluctuation in single-phase inverter system due to the instantaneous output power in H-bridge

$$\begin{aligned} p_{\mathrm{HB}} = v_{\mathrm{s}} i_{\mathrm{s}} &= \sqrt{2}U_{\mathrm{s}} \sin(\omega t) \cdot \sqrt{2}I_{\mathrm{s}} \sin(\omega t + \varphi) \\ &= U_{\mathrm{s}} I_{\mathrm{s}} \cos(\varphi) - U_{\mathrm{s}} I_{\mathrm{s}} \cos(2\omega t + \varphi) \end{aligned} \tag{3}$$

where U_{s} and I_{s} are the rms value of v_{s} and i_{s}. ωt is the phase of v_{s}. φ is the initial phase of i_{s}.

This double line-frequency power fluctuation, i.e., 100 Hz component in this article, will further give rise to the 100 Hz fluctuation in both dc-bus voltage and DAB current (both i_o and i_L). As shown in Fig. 3, the current stress of i_L under single-phase ac load is almost 2.5 times as high as that under dc load (with the same average power in a line-frequency period). The fluctuation of i_L not only deteriorates the work environment of switching devices but also increases the power losses. Therefore, the method to suppress the fluctuation of i_L is an effective means to improve the steady-state performance of DAB under single-phase ac load and steady-state condition.

Assume that the primary side dc-bus is connected to batteries in energy storage system [4] or connected in three-phase parallel to constitute a common dc-bus in the primary side of PET [14]. Therefore, the double line-frequency fluctuation in primary side dc-bus voltage v_1 under normal operation conditions is much smaller than that in secondary side dc-bus voltage v_2. Only the double line-frequency fluctuations in v_2 and i_L have been taken into consideration in this article.

The single voltage closed-loop (SVC) control method is the simplest closed-loop control strategy for DAB, as shown in Fig. 4. G_1 is the PI controller.

The propagation paths of low-frequency fluctuations in DAB are shown in Fig. 5. Superscript "$\sim$" denotes the low-frequency fluctuation components in the variable. The fluctuation components in i_o have effects on v_2, while the fluctuation components in v_2 have effects on i_o. Therefore, coupling relationship can be seen between v_2 and i_{o}. Moreover, both the fluctuation components in v_2 and δ have effects on i_L. All of these factors lead to high complexity when solving low-frequency fluctuations in analytic.

III. FLUCTUATIONS CHARACTERISTICS

A. Fluctuation Characteristics of DC-Bus Voltage

The double line-frequency components contribute most to the low-frequency ripple in voltage and current, so that the components higher than second harmonic will be neglected in following analysis. Under steady-state conditions, the following variables can be formulated as follows:

DC-bus voltage in secondary side:

$$v_2 = V_{2,\mathrm{ref}} + v_{2,\mathrm{f}} \text{ and } v_{2,\mathrm{f}} = V_{2,\mathrm{f}} \sin(2\omega t + \theta) \tag{4}$$

where the steady-state dc component is equal to reference value $V_{2,\mathrm{ref}}$. The double line-frequency fluctuation component in steady state is $v_{2,\mathrm{f}}$. θ is the initial phase of $v_{2,\mathrm{f}}$.

Output current of DAB:

$$i_\mathrm{o} = I_{\mathrm{o,dc}} + i_{\mathrm{o,f}} \text{ and } i_{\mathrm{o,f}} = I_{\mathrm{o,f}} \sin(2\omega t + \gamma) \tag{5}$$

where $I_{\mathrm{o,dc}} = U_\mathrm{s} I_\mathrm{s} \cos(\varphi)/V_{2,\mathrm{ref}}$ is the dc component in steady state, $i_{\mathrm{o,f}}$ is the double line-frequency fluctuation component in steady state. γ is the initial phase of $i_{\mathrm{o,f}}$.

The instantaneous power in ac and dc side of H-bridge should be equal (neglecting the power loss)

$$p_{\mathrm{HB}} = v_2 i_{\mathrm{load}} = v_2 i_\mathrm{o} - v_2 C \frac{dv_2}{dt}. \tag{6}$$

Substituting (3) to (5) into (6), the dc voltage fluctuation in secondary side can be solved out

$$V_{2,\mathrm{f}} = \sqrt{\frac{U_\mathrm{s}^2 I_\mathrm{s}^2 + V_{2,\mathrm{ref}}^2 I_{\mathrm{o,f}}^2 + 2U_\mathrm{s} I_\mathrm{s} V_{2,\mathrm{ref}} I_{\mathrm{o,f}} \sin(\gamma - \varphi)}{I_{\mathrm{o,dc}}^2 + 4\omega^2 C^2 V_{2,\mathrm{ref}}^2}} \tag{7}$$

where the phase angle θ of $v_{2,\mathrm{f}}$ can be calculated by

$$\cos(\theta - \gamma) = \frac{\begin{array}{c} U_\mathrm{s} I_\mathrm{s} I_{\mathrm{o,dc}} \sin(\varphi - \gamma) \\ + 2\omega C V_{2,\mathrm{ref}} U_\mathrm{s} I_\mathrm{s} \cos(\varphi - \gamma) - V_{2,\mathrm{ref}} I_{\mathrm{o,f}} I_{\mathrm{o,dc}} \end{array}}{V_{2,\mathrm{f}} I_{\mathrm{o,dc}}^2 + 4\omega^2 C^2 V_{2,\mathrm{ref}}^2 V_{2,\mathrm{f}}}$$

$$\sin(\theta - \gamma) = \frac{\begin{array}{c} -U_\mathrm{s} I_\mathrm{s} I_{\mathrm{o,dc}} \cos(\varphi - \gamma) \\ + 2\omega C V_{2,\mathrm{ref}} U_\mathrm{s} I_\mathrm{s} \sin(\varphi - \gamma) - 2\omega C V_{2,\mathrm{ref}}^2 I_{\mathrm{o,f}} \end{array}}{V_{2,\mathrm{f}} I_{\mathrm{o,dc}}^2 + 4\omega^2 C^2 V_{2,\mathrm{ref}}^2 V_{2,\mathrm{f}}}.$$

B. Fluctuation Characteristics of Phase-Shift Ratio δ

Current stress of DAB can only appear at switching moments, i.e., t_1 or t_2, as shown in (2). The phase shift ratio δ that can be solved by (1) is a square root function

$$\begin{cases} \delta = +(\frac{1}{2} - \frac{1}{2}\sqrt{1 + (-\frac{4Li_\mathrm{o}}{V_1 T_{\mathrm{hs}}})}), \ \delta \geq 0 \text{ and } 0 \leq i_\mathrm{o} \leq \frac{V_1 T_{\mathrm{hs}}}{4L} \\ \delta = -(\frac{1}{2} - \frac{1}{2}\sqrt{1 + \frac{4Li_\mathrm{o}}{V_1 T_{\mathrm{hs}}}}), \ \delta < 0 \text{ and } -\frac{V_1 T_{\mathrm{hs}}}{4L} \leq i_\mathrm{o} < 0. \end{cases} \tag{8}$$

In order to reduce the complexity of deriving the analytical expression of DAB current stress, δ should be simplified first. Equation (8) can be rewritten as the square root function $f_0 = 0.5 - 0.5(1 + x)^{1/2}$. The variable $x (= \pm(4\mathrm{L}i\mathrm{o})/(v_1 T_{\mathrm{hs}}))$ is in the range $[-1, 0]$ and the condition that $\delta = 0$ when $x = 0$ should be satisfied to avoid discontinuous zero-crossing of δ or i_o.

Linear fitting method is used to simplify f_0 into a first-order function. There is an infinite number of fitting schemes. Only three of them are given as examples shown in Fig. 6. The relative fitting errors are shown in Fig. 6(b). It can be seen that when x is close to -1 or 0, the relative fitting error becomes large. In general, the maximum power transfer capability of DAB is designed to be more than twice as the nominal power. As a result, δ and i_o are usually not very close to their maximum values. That is to say, the actual operating range of x is smaller than $[-1, 0]$.

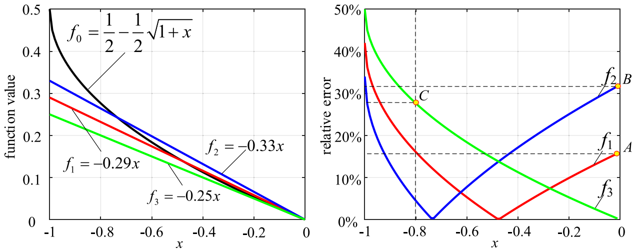

(a) (b)

Fig. 6. Linear fitting of phase shift ratio δ: (a) linear fitting function and (b) relative error of fitting.

Based on the analysis above, if the actual operating range of x is $[-0.8, 0]$, the maximum relative error of these three schemes is 15% (point A), 32% (point B), and 27% (point C), respectively. f_1 is the best fitting scheme in Fig. 6. Comparing all possible fitting schemes, the function in the following equation is selected as the appropriate fitting function in this article:

$$f_0 \approx -\frac{7}{24}x. \tag{9}$$

The fitting function in (9) covers 80% of the range of x, i.e., $[-0.8, 0]$, with maximum relative error 15% or covers 90% of the range of x, i.e., $[-0.9, 0]$, with maximum relative error 24%. The operating range of x is wide enough to cover the entire operation range of DAB with acceptable error under nominal steady-state condition.

According to (8) and (9), δ is proportional to i_o

$$\delta = \frac{7L}{6V_1 T_{\mathrm{hs}}} \cdot i_\mathrm{o}. \tag{10}$$

Equation (10) indicates that the elimination of the fluctuations in output current i_o is equivalent to the elimination of the fluctuations in phase-shift ratio δ.

C. Fluctuation Characteristics of DAB Current Stress

Based on (2), the current values of i_L at switching moments can be concluded into two forms

$$i_{\mathrm{L,p1}} = \frac{(v_2 - V_1)T_{\mathrm{hs}} + 2V_1 |\delta| T_{\mathrm{hs}}}{2L}, i_{\mathrm{L,p2}} = \frac{(V_1 - v_2)T_{\mathrm{hs}} + 2v_2 |\delta| T_{\mathrm{hs}}}{2L} \tag{11}$$

where $i_{\mathrm{L,p1}}$ is the current value when $\delta \geq 0$ and $t = t_1$ or when $\delta < 0$ and $t = t_0$. $i_{\mathrm{L,p2}}$ is the current value when $\delta \geq 0$ and $t = t_2$ or when $\delta < 0$ and $t = t_3$. Equation (11) describes the high-frequency characteristics of DAB current. It indicates that the current stress of DAB is affected by the low-frequency fluctuations both in the phase-shift δ and the dc voltage v_2.

The operating range of i_o can be classified into four different cases, i.e., $I_{\mathrm{o,dc}} \geq I_{\mathrm{o,f}} \geq 0$, $I_{\mathrm{o,f}} \geq I_{\mathrm{o,dc}} \geq 0$, $-I_{\mathrm{o,f}} \leq I_{\mathrm{o,dc}} < 0$, and $I_{\mathrm{o,dc}} \leq -I_{\mathrm{o,f}} < 0$. Taking $I_{\mathrm{o,dc}} \geq I_{\mathrm{o,f}} \geq 0$ as an example, i_o and δ are always positive in this case. Substituting (4), (5), (7), and (10) into (11), neglecting the fourth-order component, $i_{\mathrm{L,p1}}$

TABLE I
CURRENT STRESS OF DAB UNDER DOUBLE LINE-FREQUENCY FLUCTUATION WHEN $I_{\mathrm{O,DC}} \geq I_{\mathrm{O,F}} \geq 0$

Range of dc-bus voltage	$\lvert i_{\mathrm{L,p1}} \rvert_{\max}$	$\lvert i_{\mathrm{L,p2}} \rvert_{\max}$	$i_{\mathrm{L,peak}}$
$V_1 - V_{2,\mathrm{ref}} < -\frac{7LV_{2,\mathrm{ref}}}{3T_{\mathrm{hs}}V_1} I_{\mathrm{o,dc}}$	$\frac{T_{\mathrm{hs}}}{2L}(V_{2,\mathrm{ref}} - V_1) + \frac{7}{6} I_{\mathrm{o,dc}}$ $+\sqrt{A_1^2 + B_1^2 + 2A_1B_1\cos(\theta-\gamma)}$	$\frac{T_{\mathrm{hs}}}{2L}(V_{2,\mathrm{ref}} - V_1) - \frac{7V_{2,\mathrm{ref}}}{6V_1} I_{\mathrm{o,dc}}$ $+\sqrt{A_2^2 + B_2^2 + 2A_2B_2\cos(\theta-\gamma)}$	$\lvert i_{\mathrm{L,p1}} \rvert_{\max}$
$V_1 - V_{2,\mathrm{ref}} > \frac{7L}{3T_{\mathrm{hs}}} I_{\mathrm{o,dc}}$	$\frac{T_{\mathrm{hs}}}{2L}(V_1 - V_{2,\mathrm{ref}}) - \frac{7}{6} I_{\mathrm{o,dc}}$ $+\sqrt{A_1^2 + B_1^2 + 2A_1B_1\cos(\theta-\gamma)}$	$\frac{T_{\mathrm{hs}}}{2L}(V_1 - V_{2,\mathrm{ref}}) + \frac{7V_{2,\mathrm{ref}}}{6V_1} I_{\mathrm{o,dc}}$ $+\sqrt{A_2^2 + B_2^2 + 2A_2B_2\cos(\theta-\gamma)}$	$\lvert i_{\mathrm{L,p2}} \rvert_{\max}$
$-\frac{7LV_{2,\mathrm{ref}}}{3T_{\mathrm{hs}}V_1} I_{\mathrm{o,dc}} \leq V_1 - V_{2,\mathrm{ref}} \leq \frac{7L}{3T_{\mathrm{hs}}} I_{\mathrm{o,dc}}$	$\frac{T_{\mathrm{hs}}}{2L}(V_{2,\mathrm{ref}} - V_1) + \frac{7}{6} I_{\mathrm{o,dc}}$ $+\sqrt{A_1^2 + B_1^2 + 2A_1B_1\cos(\theta-\gamma)}$	$\frac{T_{\mathrm{hs}}}{2L}(V_1 - V_{2,\mathrm{ref}}) + \frac{7V_{2,\mathrm{ref}}}{6V_1} I_{\mathrm{o,dc}}$ $+\sqrt{A_2^2 + B_2^2 + 2A_2B_2\cos(\theta-\gamma)}$	$\max(\lvert i_{\mathrm{L,p1}} \rvert_{\max}, \lvert i_{\mathrm{L,p2}} \rvert_{\max})$

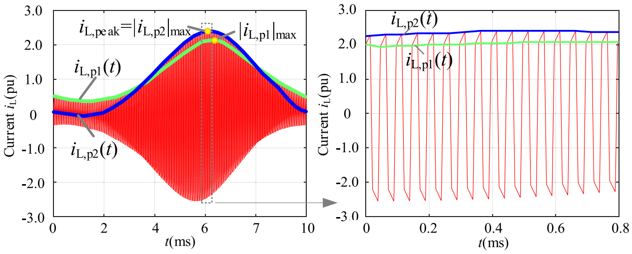

(a) (b)

Fig. 7. Current stress of DAB under low-frequency fluctuations: (a) waveforms of i_{L} and (b) details magnification.

and $i_{\mathrm{L,p2}}$, when $I_{\mathrm{o,dc}} \geq I_{\mathrm{o,f}} \geq 0$ can be derived as

$$\begin{aligned} i_{\mathrm{L,p1}}(t) &= \frac{T_{\mathrm{hs}}}{2L}(V_{2,\mathrm{ref}} - V_1) + \frac{7}{6} I_{\mathrm{o,dc}} \\ &\quad + \sqrt{A_1{}^2 + B_1{}^2 + 2A_1B_1\cos(\theta-\gamma)}\sin\left(2\omega t + \frac{\theta+\gamma}{2} + \mu_1\right) \\ i_{\mathrm{L,p2}}(t) &= \frac{T_{\mathrm{hs}}}{2L}(V_1 - V_{2,\mathrm{ref}}) + \frac{7V_{2,\mathrm{ref}}}{6V_1} I_{\mathrm{o,dc}} \\ &\quad - \sqrt{A_2{}^2 + B_2{}^2 + 2A_2B_2\cos(\theta-\gamma)}\cos\left(2\omega t + \frac{\theta+\gamma}{2} - \mu_2\right) \end{aligned} \tag{12}$$

where $A_1 = \frac{T_{\mathrm{hs}}}{2L} V_{2,\mathrm{f}}$, $B_1 = \frac{7}{6} I_{\mathrm{o,f}}$, $\mu_1 = \arctan(\frac{A_1 - B_1}{A_1 + B_1} \tan(\frac{\theta-\gamma}{2}))$, $A_2 = (\frac{T_{\mathrm{hs}}}{2L} - \frac{7}{6V_1} I_{\mathrm{o,dc}}) V_{2,\mathrm{f}}$, $B_2 = -\frac{7}{6V_1} V_{2,\mathrm{ref}} I_{\mathrm{o,f}}$, $\mu_2 = \arctan(\frac{A_2 + B_2}{A_2 - B_2} \cot(\frac{\theta-\gamma}{2}))$ As can be seen in (12), $i_{\mathrm{L,p1}}$ and $i_{\mathrm{L,p2}}$ oscillate at double line-frequency. The maximum value of $|i_{\mathrm{L,p1}}|$ and $|i_{\mathrm{L,p2}}|$, i.e., $|i_{\mathrm{L,p1}}|_{\max}$ and $|i_{\mathrm{L,p2}}|_{\max}$, can be obtained when the sinusoidal function in (12) is exactly equal to + 1 or −1. The symbol "| |" represents the absolute value. Therefore, the current stress of DAB under steady-state double line-frequency fluctuation is the maximum one of $|i_{\mathrm{L,p1}}|_{\max}$ and $|i_{\mathrm{L,p2}}|_{\max}$ as shown in the following:

$$i_{\mathrm{L,peak}} = \max(|i_{\mathrm{L,p1}}|_{\max}, \ |i_{\mathrm{L,p2}}|_{\max}). \tag{13}$$

The waveforms of i_L in DAB are shown in Figs. 3 and 7. In this case, $|i_{\mathrm{L,p2}}|_{\max}$ is larger than $|i_{\mathrm{L,p1}}|_{\max}$, so the current stress $i_{\mathrm{L,peak}}$ is equal to $|i_{\mathrm{L,p2}}|_{\max}$.

TABLE II
DAB PARAMETERS

Parameters	Nominal Value
Turn Ratio n	1
Inductance L	63uH
Switching Frequency f_s	20kHz
DC-Bus Capacitance C	400uF
DC Voltage Reference Value $V_{2,\mathrm{ref}}$	100V
DC Voltage V_1	80V~120V
DC Component of Output Current $I_{\mathrm{o,dc}}$	0~4A
Apparent Power $U_s \cdot I_s$	0~400VA
AC Current Phase φ	−π/2~+π/2

The expressions of current stress when $I_{\mathrm{o,dc}} \geq I_{\mathrm{o,f}} \geq 0$ have been derived and summarized in Table I.

It is worth noting that (11) reflects the inherent high-frequency characteristics of DAB current, while (4), (5), (7), and (10) reflect the low-frequency characteristics caused by double line-frequency power. Therefore, (12) contains both the low-frequency characteristics and high-frequency characteristics in DAB.

IV. CURRENT STRESS OPTIMIZATION METHOD BY SECOND HARMONIC CURRENT SHAPING

Under steady-state conditions, the dc component $I_{\mathrm{o,dc}}$ is determined by the average power of H-bridge and only the fluctuation component $i_{\mathrm{o,f}}$ can be controlled to reduce the current fluctuation of DAB. Therefore, $I_{\mathrm{o,f}}$ and γ are the two controllable variables which can be used to shape the second-harmonic output current of DAB. The following analysis is based on the parameters in Table II.

A. *Current Stress Optimization When* $\mathrm{V}_1 = \mathrm{V}_{2,ref}$ *and* $\mathrm{I}_{o,dc} \geq \mathrm{I}_{o,f} \geq 0$

In general, the dc components of v_1 and v_2 are set to match the turn ratio n of high-frequency transformer T, i.e., $V_1 = V_{2,\mathrm{ref}}$ in this article ($n = 1$). Under the circumstances, the reactive power in DAB can be reduced and the operation efficiency of DAB can be increased.

As shown in Fig. 8, the minimum value of current stress $i_{\mathrm{L,peak}}$ exactly locates at the intersections of $|i_{\mathrm{L,p1}}|_{\max}$ and $|i_{\mathrm{L,p2}}|_{\max}$.

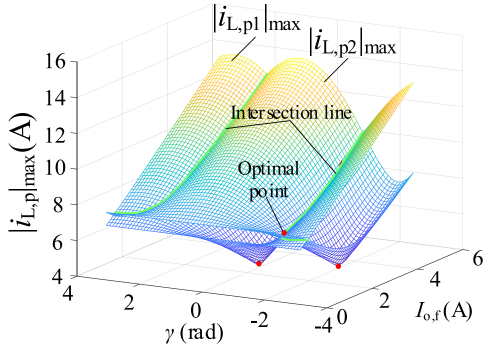

Fig. 8. $|i_{\mathrm{L,p1}}|_{\max}$ and $|i_{\mathrm{L,p2}}|_{\max}$ varied with $I_{\mathrm{o,f}}$ and γ under $V_1 = V_{2,\mathrm{ref}} = 100$ V, $U_{\mathrm{s}}I_{\mathrm{s}} = 400$ VA, and $\varphi = 0°$.

The optimal values of $I_{\mathrm{o,f}}$ and γ when $V_1 = V_{2,\mathrm{ref}}$ and $I_{\mathrm{o,dc}} \geq I_{\mathrm{o,f}} \geq 0$ are defined as $I_{\mathrm{of,opt0}}$ and γ_{opt0}. $I_{\mathrm{of,opt0}}$ and γ_{opt0} are derived as (14) and (15), respectively

$$\left.\frac{\partial |i_{\mathrm{L,p1}}|_{\max}}{\partial I_{\mathrm{o,f}}}\right|_{|i_{\mathrm{L,p1}}|_{\max}=|i_{\mathrm{L,p2}}|_{\max}} = 0$$

$$\Rightarrow I_{\mathrm{of,opt0}} = \frac{1}{\cos(\varphi)}$$

$$\sqrt{I_{\mathrm{o,dc}}^2 + 8\omega^2 C^2 V_{2,\mathrm{ref}}^2 \left(1 - \frac{\sqrt{1 + \frac{I_{\mathrm{o,dc}}^2}{4\omega^2 C^2 V_{2,\mathrm{ref}}^2}}}{\sqrt{1 + \frac{I_{\mathrm{o,dc}}^2}{4\omega^2 C^2 (V_{2,\mathrm{ref}} + \frac{49}{36 V_{2,\mathrm{ref}} A_0})^2}}}\right)} \tag{14}$$

$$\Rightarrow \begin{cases} \cos(\varphi - \gamma_{\mathrm{opt0}}) = \frac{V_{2,\mathrm{ref}}^2 I_{\mathrm{of,opt0}}^2 - {U_{\mathrm{s}}}^2 {I_{\mathrm{s}}}^2}{4\omega C V_{2,\mathrm{ref}}^2 U_{\mathrm{s}} I_{\mathrm{s}} I_{\mathrm{of,opt0}}} \cdot I_{\mathrm{o,dc}} \leq 0 \\ \sin(\varphi - \gamma_{\mathrm{opt0}}) = \sqrt{1 - (\cos(\varphi - \gamma))^2} \geq 0 \end{cases}$$

$$\Rightarrow \gamma_{\mathrm{opt0}} = \varphi - \arccos\left(\frac{V_{2,\mathrm{ref}}^2 I_{\mathrm{of,opt0}}^2 - {U_{\mathrm{s}}}^2 {I_{\mathrm{s}}}^2}{4\omega C V_{2,\mathrm{ref}}^2 I_{\mathrm{of,opt0}}} \cdot \frac{I_{\mathrm{o,dc}}}{U_{\mathrm{s}} I_{\mathrm{s}}}\right) \tag{15}$$

where $A_0 = ({T_{\mathrm{hs}}}^2/(4L^2) - (7T_{\mathrm{hs}} I_{\mathrm{o,dc}})/(12LV_{2,\mathrm{ref}}))/(I_{\mathrm{o,dc}}^2 + 4\omega^2 C^2 V_{2,\mathrm{ref}}^2)$. $I_{\mathrm{o,dc}}$ is much smaller than $4\omega^2 C^2 {V_{2,\mathrm{ref}}}^2$ and $4\omega^2 C^2 (V_{2,\mathrm{ref}} + 49/36/V_{2,\mathrm{ref}}/A_0)^2$, so the Taylor's linear approximation $(1 + x)^{1/2} \approx 1 + 0.5x$ when $x \rightarrow 0$ can be used to simplify (14) to be as follows:

$$I_{\mathrm{of,opt0}} \approx \frac{U_{\mathrm{s}} I_{\mathrm{s}}}{V_{2,\mathrm{ref}}} \sqrt{\frac{I_{\mathrm{o,dc}}^2 + k_1}{I_{\mathrm{o,dc}}^2 + k_2}} \approx \frac{U_{\mathrm{s}} I_{\mathrm{s}}}{V_{2,\mathrm{ref}}} \sqrt{\frac{I_{\mathrm{odc,N}}^2 \big/ 4 + k_1}{I_{\mathrm{odc,N}}^2 \big/ 4 + k_2}} \tag{16}$$

where $k_1 = 8\omega^2 C^2 {V_{2,\mathrm{ref}}}^2$, $k_2 = 8\omega^2 C^2 (V_{2,\mathrm{ref}} + 49/36/V_{2,\mathrm{ref}}/A_0)^2$. It can be found that $I_{\mathrm{o,dc}}$ is generally much smaller than k_1 and k_2. Therefore, (16) is not sensitive to the variation of $I_{\mathrm{o,dc}}$. In this article, $I_{\mathrm{o,dc}}$ in (16) and A_0(i.e., k_2) both are set as a constant exactly to be half of its nominal value, i.e., $I_{\mathrm{odc,N}}/2$, to reduce approximation deviation by (16). As a result, $I_{\mathrm{of,opt0}}$ becomes a function of $U_{\mathrm{s}}I_{\mathrm{s}}$. Substituting (16) into (15), γ_{opt0} becomes a function of $I_{\mathrm{o,dc}}$. The computation complexity can be reduced.

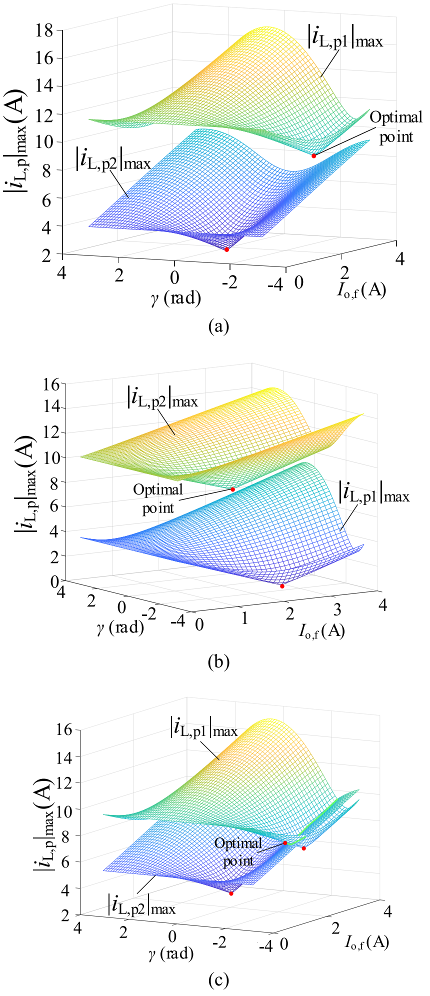

(a)

(b)

(c)

Fig. 9. $|i_{\mathrm{L,p1}}|_{\max}$ and $|i_{\mathrm{L,p2}}|_{\max}$ varied with $I_{\mathrm{o,f}}$ and γ under $V_1 \neq V_{2,\mathrm{ref}} = 100$ V, $U_{\mathrm{s}}I_{\mathrm{s}} = 400$ VA, and $\varphi = 0°$. (a) Case I: $V_1 = 80$ V. (b) Case II: $V_1 = 120$ V. (c) Case III: $V_1 = 90$ V.

B. Current Stress Optimization When $V_1 \neq V_{2,ref}$ *and* $I_{o,dc} \geq I_{o,f} \geq 0$

In some cases, V_1 may deviate from $V_{2,\mathrm{ref}}$ slightly, e.g., the battery voltage will change with its state of charge. In these cases, the method in Section IV-A may not be valid anymore.

Actually, the location relationships in three-dimensional space of the curved surfaces $|i_{\mathrm{L,p1}}|_{\max}$ and $|i_{\mathrm{L,p2}}|_{\max}$ can be classified into three different cases, as shown in Fig. 9:

Case I: $|i_{\mathrm{L,p1}}|_{\max}$ is larger than $|i_{\mathrm{L,p2}}|_{\max}$ at every point. $|i_{\mathrm{L,p1}}|_{\max}$ and $|i_{\mathrm{L,p2}}|_{\max}$ have no intersections. The minimum point of $|i_{\mathrm{L,p1}}|_{\max}$ is the optimal point, as shown in Fig. 9(a).

Case II: $|i_{\mathrm{L,p1}}|_{\max}$ is smaller than $|i_{\mathrm{L,p2}}|_{\max}$ at every point. $|i_{\mathrm{L,p1}}|_{\max}$ and $|i_{\mathrm{L,p2}}|_{\max}$ have no intersections. The minimum point of $|i_{\mathrm{L,p2}}|_{\max}$ is the optimal point, as shown in Fig. 9(b).

Case III: $|i_{\mathrm{L,p1}}|_{\max}$ and $|i_{\mathrm{L,p2}}|_{\max}$ have intersections. The optimal point locates at the points of intersection, similar to the case when $V_1 = V_{2,\mathrm{ref}}$, as shown in Fig. 9(c).

In case I, the minimum point of $|i_{\mathrm{L,p1}}|_{\max}$ is the optimal point. The optimal values of $I_{\mathrm{o,f}}$ and γ in case I are defined as $I_{\mathrm{of,opt1}}$

and γ_{opt1}. $I_{\mathrm{of,opt1}}$ and γ_{opt1} can be derived as follows:

$$\begin{aligned}
&\frac{\partial|i_{\mathrm{L,p1}}|_{\max}}{\partial\gamma}=0,\ \frac{\partial|i_{\mathrm{L,p1}}|_{\max}}{\partial I_{\mathrm{o,f}}}=0\\
&\Rightarrow\begin{cases} I_{\mathrm{of,opt1}}=\dfrac{\frac{T_{\mathrm{hs}}}{2L}U_{\mathrm{s}}I_{\mathrm{s}}}{\sqrt{(\frac{7}{3}\omega CV_{2,\mathrm{ref}})^2+(\frac{7}{6}I_{\mathrm{o,dc}}-\frac{T_{\mathrm{hs}}}{2L}V_{2,\mathrm{ref}})^2}}\\ \gamma_{\mathrm{opt1}}=\varphi-\arccos\left(\dfrac{-\frac{7}{3}\omega CV_{2,\mathrm{ref}}}{\sqrt{(\frac{7}{3}\omega CV_{2,\mathrm{ref}})^2+(\frac{7}{6}I_{\mathrm{o,dc}}-\frac{T_{\mathrm{hs}}}{2L}V_{2,\mathrm{ref}})^2}}\right)\end{cases}\\
&\xrightarrow{\text{simplify}}\begin{cases} I_{\mathrm{of,opt1}}\approx k_3U_{\mathrm{s}}I_{\mathrm{s}}\\ \gamma_{\mathrm{opt1}}\approx\varphi-\arccos(k_4)\end{cases}\\
&k_3=\frac{\frac{T_{\mathrm{hs}}}{2L}}{\sqrt{(\frac{7}{3}\omega CV_{2,\mathrm{ref}})^2+(\frac{7}{12}I_{\mathrm{odc,N}}-\frac{T_{\mathrm{hs}}}{2L}V_{2,\mathrm{ref}})^2}}\\
&k_4=\frac{-\frac{7}{3}\omega CV_{2,\mathrm{ref}}}{\sqrt{(\frac{7}{3}\omega CV_{2,\mathrm{ref}})^2+(\frac{7}{12}I_{\mathrm{odc,N}}-\frac{T_{\mathrm{hs}}}{2L}V_{2,\mathrm{ref}})^2}}
\end{aligned}\tag{17}$$

where $I_{\mathrm{of,opt1}}$ and γ_{opt1} are irrelative to V_1. Moreover, $I_{\mathrm{o,dc}}$ is much smaller than ($3T_{\mathrm{hs}}V_{2,\mathrm{ref}}$)/(7L). Equation (17) is not sensitive to the variation of $I_{\mathrm{o,dc}}$ and $I_{\mathrm{o,dc}}$ can be set as a constant exactly to be half of its nominal value. k_3 and k_4 are constant coefficients which are calculated offline. In this way, $I_{\mathrm{of,opt1}}$ can be simplified as a function of $U_{\mathrm{s}}I_{\mathrm{s}}$ and γ_{opt1} can be simplified as a function of φ

$$\begin{aligned}
&|i_{\mathrm{L,p1}}|_{\max}\Big|_{I_{\mathrm{o,f}}=I_{\mathrm{of,opt1}},\gamma=\gamma_{\mathrm{opt1}}}=|i_{\mathrm{L,p2}}|_{\max}\Big|_{I_{\mathrm{o,f}}=I_{\mathrm{of,opt1}},\gamma=\gamma_{\mathrm{opt1}}}\\
&\Rightarrow V_{1,\lim 1}=-\frac{L}{2T_{\mathrm{hs}}}\left(\frac{7}{6}I_{\mathrm{of,opt1}}-\frac{T_{\mathrm{hs}}}{L}V_{2,\mathrm{ref}}-\frac{7}{6}I_{\mathrm{o,dc}}\right)\\
&+\frac{L}{2T_{\mathrm{hs}}}\sqrt{\underbrace{\left(\frac{7}{6}I_{\mathrm{o,dc}}+\frac{7}{2}I_{\mathrm{of,opt1}}-\frac{T_{\mathrm{hs}}}{L}V_{2,\mathrm{ref}}\right)^2}_{\text{part A}}\underbrace{-\frac{98}{9}I_{\mathrm{of,opt1}}}_{\text{part B}}}\\
&\xrightarrow{\text{simplify}}\ V_{1,\mathrm{lim1}}=V_{2,\mathrm{ref}}-\frac{7L}{3T_{\mathrm{hs}}}I_{\mathrm{of,opt1}}
\end{aligned}\tag{18}$$

The boundary condition of case I and case III is the voltage $V_1=V_{1,\mathrm{lim1}}$ when $|i_{\mathrm{L,p1}}|_{\max}$ is exactly equal to $|i_{\mathrm{L,p2}}|_{\max}$ at the minimum point of $|i_{\mathrm{L,p1}}|_{\max}$. $V_{1,\mathrm{lim1}}$ can be derived as (18).

In (18), part A under the square root is much larger than the part B. Therefore, (18) can be simplified as a linear function of $I_{\mathrm{of,opt1}}$.

In case II, the minimum point of $|i_{\mathrm{L,p2}}|_{\max}$ is the optimal point. Similar to the derivation process in case I, the optimal value of $I_{\mathrm{o,f}}$ and γ in case II are defined as $I_{\mathrm{of,opt2}}$ and γ_{opt2}. $I_{\mathrm{of,opt2}}$ and γ_{opt2} can be derived as follows:

$$\begin{aligned}
&\frac{\partial|i_{\mathrm{L,p2}}|_{\max}}{\partial\gamma}\\
&\quad=0,\ \frac{\partial|i_{\mathrm{L,p2}}|_{\max}}{\partial I_{\mathrm{o,f}}}=0\\
&\Rightarrow\begin{cases} I_{\mathrm{of,opt2}}=\dfrac{U_{\mathrm{s}}I_{\mathrm{s}}(\frac{T_{\mathrm{hs}}}{2L}V_1-\frac{7}{6}I_{\mathrm{o,dc}})}{V_{2,\mathrm{ref}}\sqrt{\frac{T_{\mathrm{hs}}{}^2}{4L^2}V_1{}^2+\frac{49}{9}\omega^2C^2V_{2,\mathrm{ref}}^2}}\\ \gamma_{\mathrm{opt2}}=\varphi-\arccos\left(\dfrac{\frac{7}{3}\omega CV_{2,\mathrm{ref}}}{\sqrt{\frac{T_{\mathrm{hs}}{}^2}{4L^2}V_1{}^2+\frac{49}{9}\omega^2C^2V_{2,\mathrm{ref}}^2}}\right)\end{cases}\\
&\xrightarrow{\text{simplify}}\begin{cases} I_{\mathrm{of,opt2}}\approx(k_5V_1-k_6I_{\mathrm{o,dc}})U_{\mathrm{s}}I_{\mathrm{s}}\\ \gamma_{\mathrm{opt2}}\approx\varphi-\arccos(k_7)\end{cases}\\
&k_6=\frac{7}{6V_{2,\mathrm{ref}}^2\sqrt{\frac{T_{\mathrm{hs}}{}^2}{4L^2}+\frac{49}{9}\omega^2C^2}},\ k_5=\frac{3T_{\mathrm{hs}}}{7L}k_6,\ k_7=2\omega CV_{2,\mathrm{ref}}^2k_6.
\end{aligned}\tag{19}$$

Assume that V_1 does not deviate from $V_{2,\mathrm{ref}}$ too much (e.g., the deviation between V_1 and $V_{2,\mathrm{ref}}$ is smaller than ±20%), so V_1 under the square root can be substituted by $V_{2,\mathrm{ref}}$ to reduce computation complexity without large error. As a result, the mathematical operation of square root is removed in (19) and γ_{opt2} is simplified as a function of φ. k_5 to k_7 are constant coefficients which are calculated offline.

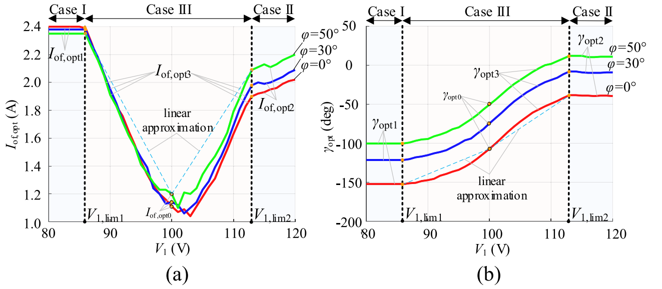

(a) (b)

Fig. 10. $I_{\mathrm{of,opt}}$ and γ_{opt} varied with V_1 under different φ, $V_{2,\mathrm{ref}}=100$ V and $U_{\mathrm{s}}I_{\mathrm{s}}=400$ VA. (a) $I_{\mathrm{of,opt}}$ varied with V_1 under different φ. (b) γ_{opt} varied with V_1 under different φ.

The boundary condition of case II and case III is the voltage $V_1=V_{1,\mathrm{lim2}}$ when $|i_{\mathrm{L,p2}}|_{\max}$ is exactly equal to $|i_{\mathrm{L,p1}}|_{\max}$ at the minimum point of $|i_{\mathrm{L,p2}}|_{\max}$. $V_{1,\mathrm{lim2}}$ can be calculated by

$$\begin{aligned}
&|i_{\mathrm{L,p2}}|_{\max}\Big|_{I_{\mathrm{o,f}}=I_{\mathrm{of,opt2}},\gamma=\gamma_{\mathrm{opt2}}}\\
&=|i_{\mathrm{L,p1}}|_{\max}\Big|_{I_{\mathrm{o,f}}=I_{\mathrm{of,opt2}},\gamma=\gamma_{\mathrm{opt2}}}\\
&\Rightarrow V_{1,\lim 2}\approx(1+k_6U_{\mathrm{s}}I_{\mathrm{s}})V_{2,\mathrm{ref}}
\end{aligned}\tag{20}$$

where $V_{1,\mathrm{lim2}}$ is simplified as a function of $U_{\mathrm{s}}I_{\mathrm{s}}$.

In case III, the optimal point locates at the intersections of $|i_{\mathrm{L,p1}}|_{\max}$ and $|i_{\mathrm{L,p2}}|_{\max}$, just like the case when $V_1=V_{2,\mathrm{ref}}$ in Section IV-A. The optimal value of $I_{\mathrm{o,f}}$ and γ in case III are defined as $I_{\mathrm{of,opt3}}$ and γ_{opt3}. However, it is too complicated to derive the analytical expressions of $I_{\mathrm{of,opt3}}$ and γ_{opt3} when $V_1\neq V_{2,\mathrm{ref}}$.

Actually, based on the equations in Table I, the optimal values of $I_{\mathrm{o,f}}$ and γ, i.e., $I_{\mathrm{of,opt}}$ and γ_{opt}, can be solved by numerical optimization methods with the help of common mathematical tool software, e.g., MATLAB. In order to achieve online real-time calculation of $I_{\mathrm{of,opt3}}$ and γ_{opt3} based on analytical expressions rather than high-dimensional lookup table, the value of $I_{\mathrm{of,opt}}$ and γ_{opt} varied with V_1 are plotted first by numerical optimization method to form curves as shown in Fig. 10. Then, some approximations and simplifications can be made to derive the analytical expressions.

As shown in Fig. 10, when $V_1<V_{1,\mathrm{lim1}}$, DAB works in case I; when $V_1>V_{1,\mathrm{lim2}}$, DAB works in case II; when $V_{1,\mathrm{lim1}}\leq V_1\leq V_{1,\mathrm{lim2}}$, DAB works in case III.

In case I, $I_{\mathrm{of,opt1}}$ and γ_{opt1} do not change with V_1 while $I_{\mathrm{of,opt1}}$ just slightly changes with $I_{\mathrm{o,dc}}$(or φ). It validates the availability and effectiveness of the simplifications in (17).

In case II, $I_{\mathrm{of,opt2}}$ exhibits linear relation with V_1. γ_{opt2} just slightly changes with V_1. It validates the availability and effectiveness of the simplifications in (19).

In case III, $I_{\mathrm{of,opt0}}$ just slightly changes with $I_{\mathrm{o,dc}}$(or φ). It validates the availability and effectiveness of the simplifications in (16).

In case III, $I_{\mathrm{of,opt3}}$ exhibits good linear relation with V_1 in the two ranges $V_1<V_{2,\mathrm{ref}}$ and $V_1>V_{2,\mathrm{ref}}$, respectively. Therefore, linear approximation can be made to calculate $I_{\mathrm{of,opt3}}$ in the two ranges, respectively. The similar linear approximation can also be made to calculate γ_{opt3} in the two ranges, respectively. As a result, $I_{\text{of,opt3}}$ and γ_{opt3} can be calculated approximately by

$$I_{\text{of,opt3}} = \begin{cases} \text{When } V_{1,\text{lim}\,1} \le V_1 \le V_{2,\text{ref}}: \\ I_{\text{of,opt1}} + \frac{I_{\text{of,opt0}} - I_{\text{of,opt1}}}{V_{2,\text{ref}} - V_{1,\text{lim}\,1}} (V_1 - V_{1,\text{lim}\,1}) \\ \text{When } V_{2,\text{ref}} \le V_1 \le V_{1,\text{lim}\,2}: \\ I_{\text{of,opt2}}|_{V_1 = V_{1,\text{lim}\,2}} \\ + \frac{I_{\text{of,opt0}} - I_{\text{of,opt2}}|_{V_1 = V_{1,\text{lim}\,2}}}{V_{2,\text{ref}} - V_{1,\text{lim}\,2}} (V_1 - V_{1,\text{lim}\,2}) \end{cases} \tag{21a}$$

$$\gamma_{\text{opt3}} = \begin{cases} \text{When } V_{1,\text{lim}\,1} \le V_1 \le V_{2,\text{ref}}: \\ \gamma_{\text{opt1}} + \frac{\gamma_{\text{opt0}} - \gamma_{\text{opt1}}}{V_{2,\text{ref}} - V_{1,\text{lim}\,1}} (V_1 - V_{1,\text{lim}\,1}) \\ \text{When } V_{2,\text{ref}} \le V_1 \le V_{1,\text{lim}\,2}: \\ \gamma_{\text{opt2}} + \frac{\gamma_{\text{opt0}} - \gamma_{\text{opt2}}}{V_{2,\text{ref}} - V_{1,\text{lim}\,2}} (V_1 - V_{1,\text{lim}\,2}) \end{cases} \tag{21b}$$

where $I_{\text{of,opt0}}(\gamma_{\text{opt0}})$, $I_{\text{of,opt1}}(\gamma_{\text{opt1}})$, and $I_{\text{of,opt2}}(\gamma_{\text{opt2}})$ can be calculated by (15)–(20). The high-dimensional lookup table can be avoided.

C. *Current Stress Optimization When $\varphi = \pm 90°$ and $I_{o,f} \ge I_{o,dc} \ge 0$*

When φ approaches ±90°, the optimal value of $I_{\text{o,f}}$ may become larger than $I_{\text{o,dc}}$. In this case, δ will become negative in part of one double line-frequency period. According to (11), the values of $i_{\text{L,p1}}$ and $i_{\text{L,p2}}$ are supposed to be calculated in two ranges when $\delta \ge 0$ and $\delta < 0$, respectively, as shown in (22).

Compared to the expressions (12) when $I_{\text{o,dc}} \ge I_{\text{o,f}} \ge 0$, two more expressions of $i_{\text{L,p1}}$ and $i_{\text{L,p2}}$ should be considered to derive the current stress $i_{\text{L,peak}}$ when $I_{\text{o,f}} \ge I_{\text{o,dc}} \ge 0$. As a result, the derivation process of $i_{\text{L,peak}}$ when $I_{\text{o,f}} \ge I_{\text{o,dc}} \ge 0$ is much more complicated than the derivation process when $I_{\text{o,dc}} \ge I_{\text{o,f}} \ge 0$. It is too complicated to solve the extreme value directly among the four expressions in (22) by analytical method directly.

$$\text{When } \delta \ge 0 \Rightarrow -\arcsin\left(\frac{I_{\text{o,dc}}}{I_{\text{o,f}}}\right) \le 2\omega t + \gamma \le \pi + \arcsin\left(\frac{I_{\text{o,dc}}}{I_{\text{o,f}}}\right)$$

$$\begin{cases} i_{\text{L,p1}}(t) = \frac{T_{\text{hs}}}{2L}(V_{2,\text{ref}} - V_1) + \frac{7}{6} I_{\text{o,dc}} \\ + \sqrt{{A_1}^2 + {B_1}^2 + 2A_1 B_1 \cos(\theta - \gamma)} \sin(2\omega t + \frac{\theta + \gamma}{2} + \mu_1) \\ i_{\text{L,p2}}(t) = \frac{T_{\text{hs}}}{2L}(V_1 - V_{2,\text{ref}}) + \frac{7V_{2,\text{ref}}}{6V_1} I_{\text{o,dc}} \\ - \sqrt{{A_2}^2 + {B_2}^2 + 2A_2 B_2 \cos(\theta - \gamma)} \cos(2\omega t + \frac{\theta + \gamma}{2} - \mu_2) \end{cases}$$

$$A_1 = \frac{T_{\text{hs}}}{2L} V_{2,\text{f}}, B_1 = \frac{7}{6} I_{\text{o,f}},$$

$$\mu_1 = \arctan\left(\frac{A_1 - B_1}{A_1 + B_1} \tan\left(\frac{\theta - \gamma}{2}\right)\right)$$

$$A_2 = \left(\frac{T_{\text{hs}}}{2L} - \frac{7}{6V_1} I_{\text{o,dc}}\right) V_{2,\text{f}}, B_2 = -\frac{7}{6V_1} V_{2,\text{ref}} I_{\text{o,f}},$$

$$\mu_2 = \arctan\left(\frac{A_2 + B_2}{A_2 - B_2} \cot\left(\frac{\theta - \gamma}{2}\right)\right).$$

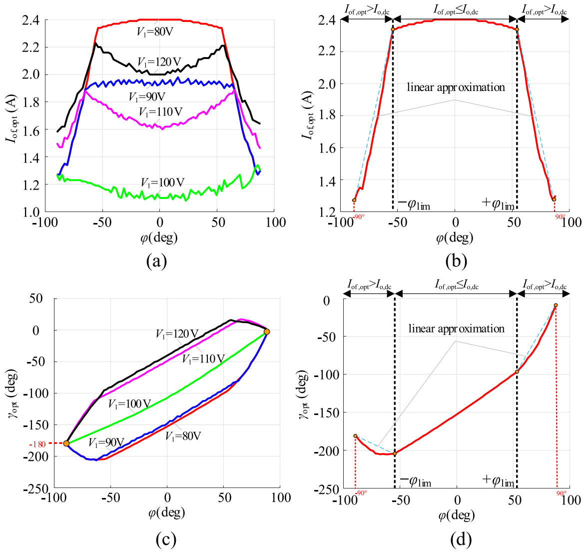

Fig. 11. $I_{\text{of,opt}}$ and γ_{opt} varied with φ under different V_1 and $V_{2,\text{ref}} = 100$ V, $U_{\text{s}} I_{\text{s}} = 400$ VA. (a) $I_{\text{of,opt}}$ varied with φ under different V_1. (b) $I_{\text{of,opt}}$ varied with φ when $V_1 = 80$ V. (c) γ_{opt} varied with φ under different V_1. (d) γ_{opt} varied with φ when $V_1 = 80$ V.

$$\text{When } \delta < 0 \Rightarrow \pi + \arcsin\left(\frac{I_{\text{o,dc}}}{I_{\text{o,f}}}\right) \le 2\omega t + \gamma \le 2\pi - \arcsin\left(\frac{I_{\text{o,dc}}}{I_{\text{o,f}}}\right)$$

$$\begin{cases} i_{\text{L,p1}}(t) = \frac{T_{\text{hs}}}{2L}(V_{2,\text{ref}} - V_1) - \frac{7}{6} I_{\text{o,dc}} \\ + \sqrt{{A_3}^2 + {B_3}^2 + 2A_3 B_3 \cos(\theta - \gamma)} \cos(2\omega t + \frac{\theta + \gamma}{2} - \mu_3) \\ i_{\text{L,p2}}(t) = \frac{T_{\text{hs}}}{2L}(V_1 - V_{2,\text{ref}}) - \frac{7V_{2,\text{ref}}}{6V_1} I_{\text{o,dc}} \\ - \sqrt{{A_4}^2 + {B_4}^2 + 2A_4 B_4 \cos(\theta - \gamma)} \sin(2\omega t + \frac{\theta + \gamma}{2} + \mu_4) \end{cases}$$

$$A_3 = \frac{T_{\text{hs}}}{2L} V_{2,\text{f}}, B_3 = -\frac{7}{6} I_{\text{o,f}},$$

$$\mu_3 = \arctan\left(\frac{A_3 + B_3}{A_3 - B_3} \cot\left(\frac{\theta - \gamma}{2}\right)\right)$$

$$A_4 = \left(\frac{7}{6V_1} I_{\text{o,dc}} + \frac{T_{\text{hs}}}{2L}\right) V_{2,\text{f}}, B_4 = \frac{7}{6V_1} V_{2,\text{ref}} I_{\text{o,f}},$$

$$\mu_4 = \arctan\left(\frac{A_4 - B_4}{A_4 + B_4} \tan\left(\frac{\theta - \gamma}{2}\right)\right). \tag{22}$$

Based on (22), the numerical optimal results reveal that γ_{opt} is equal to 0 when $\varphi = +\pi/2$ and γ_{opt} is equal to $-\pi$ when $\varphi = -\pi/2$, as shown in Fig. 11(c). Based on the numerical optimization results, the condition $\varphi = +\pi/2$, $\gamma_{\text{opt}} = 0$ or $\varphi = -\pi/2$, $\gamma_{\text{opt}} = -\pi$ is substituted into (22), so the analytical expressions of current stress $i_{\text{L,peak}}$ can be derived as

$$i_{\text{L,peak}} = \begin{cases} |i_{\text{L,p1}}|_{\max} = \frac{T_{\text{hs}}}{2L}(V_{2,\text{ref}} - V_1) & V_1 < V_{2,\text{ref}} \\ + \sqrt{\frac{{T_{\text{hs}}}^2}{4L^2} V_{2,\text{f}}^2 + \frac{49}{36} I_{\text{o,f}}^2}, & \\ |i_{\text{L,p2}}|_{\max} = \frac{T_{\text{hs}}}{2L}(V_1 - V_{2,\text{ref}}) & V_1 \ge V_{2,\text{ref}} \\ + \sqrt{\frac{{T_{\text{hs}}}^2}{4L^2} V_{2,\text{f}}^2 + \frac{49}{36{V_1}^2} V_{2,\text{ref}}^2 I_{\text{o,f}}^2}, & \end{cases}. \tag{23}$$

Based on (23), $I_{\mathrm{of,opt4}}$ and γ_{opt4} are solved as (24) shown at the bottom of this page, where $I_{\mathrm{of,opt4}}$ and γ_{opt4} are the optimization results of $I_{\mathrm{o,f}}$ and γ_{opt} when $\varphi = \pm\pi/2$. $I_{\mathrm{of,opt4}}$ is a function of $U_{\mathrm{s}}I_{\mathrm{s}}$ when $V_1 < V_{2,\mathrm{ref}}$. $I_{\mathrm{of,opt4}}$ is a function of V_1 and $U_{\mathrm{s}}I_{\mathrm{s}}$ when $V_1 \geq V_{2,\mathrm{ref}}$. γ_{opt4} is constant.

D. Current Stress Optimization When $\varphi \neq \pm 90°$ and $\mathrm{I}_{o,f} \geq \mathrm{I}_{o,dc} \geq 0$

The values of $I_{\mathrm{of,opt}}$ and γ_{opt} varied with φ under different V_1 are depicted in Fig. 11 by numerical optimization method.

Under a given value of V_1, $I_{\mathrm{of,opt}}$ and γ_{opt} can be divided into three segments according to φ_{lim}.

When $-\varphi_{\mathrm{lim}} \leq \varphi \leq +\varphi_{\mathrm{lim}}$, $I_{\mathrm{of,opt}}$ is smaller than $I_{\mathrm{o,dc}}$. $I_{\mathrm{of,opt}}$ and γ_{opt} can be calculated by the method in Section IV-A and IV-B.

When $\varphi < -\varphi_{\mathrm{lim}}$ or $\varphi > +\varphi_{\mathrm{lim}}$, $I_{\mathrm{of,opt}}$ is larger than $I_{\mathrm{o,dc}}$. The method in Section IV-A and IV-B cannot be valid anymore. However, $I_{\mathrm{of,opt}}$ and γ_{opt} exhibit good linear relation with φ. Therefore, linear approximation can also be made to calculate $I_{\mathrm{of,opt}}$ and γ_{opt} in the two segments, respectively.

The key to solve $I_{\mathrm{of,opt}}$ and γ_{opt} when $I_{\mathrm{o,f}} \geq I_{\mathrm{o,dc}} \geq 0$ is the value of φ_{lim}.

When $V_1 < V_{1,\mathrm{lim1}}$, DAB works in case I. Set $I_{\mathrm{of,opt1}} = I_{\mathrm{o,dc}}$ in (17) to solve φ_{lim}.

When $V_1 > V_{1,\mathrm{lim2}}$, DAB works in case II; Set $I_{\mathrm{of,opt2}} = I_{\mathrm{o,dc}}$ in (19) to solve φ_{lim}.

When $V_{1,\mathrm{lim1}} \leq V_1 \leq V_{1,\mathrm{lim2}}$, DAB works in case III. Set $I_{\mathrm{of,opt3}} = I_{\mathrm{o,dc}}$ in (21) to solve φ_{lim}.

Based on (16), (17), (19), and (21), φ_{lim} can be derived as

When $V_1 < V_{1,\mathrm{lim1}}$:

$\varphi_{\mathrm{lim}} = +\arccos(k_3 V_{2,\mathrm{ref}})$.

When $V_1 > V_{1,\mathrm{lim2}}$

$$\varphi_{\mathrm{lim}} = +\arccos\left(\frac{k_5 V_{2,\mathrm{ref}} V_1}{1 + k_6 U_{\mathrm{s}} I_{\mathrm{s}}}\right).$$

When $V_{1,\mathrm{lim1}} \leq V_1 \leq V_{2,\mathrm{ref}}$

$$\varphi_{\mathrm{lim}} = + \arccos\left(\frac{(\sqrt{\frac{k_1}{k_2}} - k_3 V_{2,\mathrm{ref}})V_1 + k_3 V_{2,\mathrm{ref}}^2 - \sqrt{\frac{k_1}{k_2}} V_{1,\lim 1}}{V_{2,\mathrm{ref}} - V_{1,\lim 1}}\right).$$

When $V_{2,\mathrm{ref}} \leq V_1 \leq V_{1,\mathrm{lim2}}$

$$\varphi_{\mathrm{lim}} = +\arccos \left(\frac{\left(\sqrt{\frac{k_1}{k_2}} - k_5 V_{2,\mathrm{ref}} V_{1,\lim 2}\right) V_1 + V_{1,\lim 2}(k_5 V_{2,\mathrm{ref}}^2 - \sqrt{\frac{k_1}{k_2}})}{V_{2,\mathrm{ref}} - V_{1,\lim 2}}\right). \tag{25}$$

TABLE III
BOUNDARY VALUES OF φ AND V_1

	φ_{lim}
$V_1 < V_{1,\mathrm{lim1}}$	$\varphi_{\mathrm{lim}} = 0.9521$
$V_1 > V_{1,\mathrm{lim2}}$	$\varphi_{\mathrm{lim}} = \arccos(\frac{(5.604\text{e-}3)V_1}{1+(3.295\text{e-}04)U_{\mathrm{s}}I_{\mathrm{s}}})$
$V_{1,\mathrm{lim1}} \leq V_1 \leq V_{2,\mathrm{ref}}$	$\varphi_{\mathrm{lim}} = \arccos(\frac{-8.607V_1 + 860.7}{U_{\mathrm{s}}I_{\mathrm{s}}} + 0.2865)$
$V_{2,\mathrm{ref}} < V_1 \leq V_{1,\mathrm{lim2}}$	$\varphi_{\mathrm{lim}} = \arccos(\frac{8.301V_1 - 830.1}{U_{\mathrm{s}}I_{\mathrm{s}}} + (5.604\text{e-}3)V_1 - 0.2739)$
$V_{1,\mathrm{lim1}}$=100-0.0341$U_{\mathrm{s}}I_{\mathrm{s}}$ $V_{1,\mathrm{lim2}}$=100+0.0330$U_{\mathrm{s}}I_{\mathrm{s}}$	

$I_{\mathrm{of,opt}}$ and γ_{opt} when $I_{\mathrm{o,f}} \geq I_{\mathrm{o,dc}} \geq 0$ can be solved by linear approximation as shown in (26) and (27) shown at the bottom of the next page.

E. Implementation Method

Based on the parameters in Table II, φ_{lim} can be calculated by the equations in Table III and the optimal values of $I_{\mathrm{o,f}}$ and γ can be calculated by the equations in Tables IV and V (on the next page). It can be seen from Tables III–V that these equations can be simplified to be functions of $U_{\mathrm{s}}I_{\mathrm{s}}$, φ, and V_1 by substituting the actual parameters into (14)–(25). The coefficients in these equations can be regarded as constant during its design lifetime and can be calculated offline.

The online calculation process of SHCS method is summarized in Fig. 12(a). The first step is to calculate the boundary values of V_1, i.e., $V_{1,\mathrm{lim1}}$ and $V_{1,\mathrm{lim2}}$. The second step is to calculate the boundary value of φ, i.e., φ_{lim}. The third step is to judge the ranges in which V_1 and φ located, then $I_{\mathrm{of,opt}}$ and γ_{opt} can be calculated.

Table IV covers most of the range of $\varphi(|\varphi| \leq \varphi_{\mathrm{lim}})$, especially when V_1 is close to $V_{2,\mathrm{ref}}$ (e.g., $\varphi_{\mathrm{lim}} = 73°$ when $V_1 = V_{2,\mathrm{ref}}$). In many applications, converters are designed to operate at nearby the unit power factor, so only the equations in Table IV are needed to be calculated in these cases. The most complicated part in the online calculation process of SHCS method is Table V when $|\varphi| > \varphi_{\mathrm{lim}}$.

A simplification can be made that $I_{\mathrm{o,f}}$ is forced to be equal to $I_{\mathrm{o,dc}}$ when $|\varphi| > \varphi_{\mathrm{lim}}$. As a result, only the operating condition $I_{\mathrm{o,dc}} \geq I_{\mathrm{o,f}} \geq 0$ is engaged and Table V is abandoned. In this case, only γ should be optimized. It can be derived that the optimized results of γ when $I_{\mathrm{o,f}} = I_{\mathrm{o,dc}}$ and $|\varphi| > \varphi_{\mathrm{lim}}$ are the same as that when $|\varphi| \leq \varphi_{\mathrm{lim}}$. Therefore, Table IV is valid both when $|\varphi| \leq \varphi_{\mathrm{lim}}$ and $|\varphi| > \varphi_{\mathrm{lim}}$ under this simplification ($I_{\mathrm{o,f}} = I_{\mathrm{o,dc}}$). However, the optimization effects of simplified SHCS method (SSHCS) are poorer than that of SHCS method when $|\varphi| > \varphi_{\mathrm{lim}}$. The online calculation process of is shown in Fig. 12(b).

$$I_{\mathrm{of,opt4}} = \begin{cases} \dfrac{\frac{U_{\mathrm{s}} I_{\mathrm{s}}}{V_{2,\mathrm{ref}}}}{1+\frac{196}{9{T_{\mathrm{hs}}}^2}\omega^2 L^2 C^2}, & V_1 < V_{2,\mathrm{ref}}, \varphi = \pm\frac{\pi}{2} \\ \dfrac{\frac{U_{\mathrm{s}} I_{\mathrm{s}}}{V_{2,\mathrm{ref}}}}{1+\frac{196 V_{2,\mathrm{ref}}^2}{9{T_{\mathrm{hs}}}^2 V_1^2}\omega^2 L^2 C^2}, & V_1 \geq V_{2,\mathrm{ref}}, \varphi = \pm\frac{\pi}{2} \end{cases} \quad \gamma_{\mathrm{opt4}} = \begin{cases} 0, & \varphi = +\frac{\pi}{2} \\ -\pi, & \varphi = -\frac{\pi}{2} \end{cases} \tag{24}$$

TABLE IV
OPTIMAL VALUES OF $I_{\mathrm{O,F}}$ AND γ WHEN $-\varphi_{\mathrm{LIM}} \leq \varphi \leq +\varphi_{\mathrm{LIM}}$

	$I_{\mathrm{of,opt}}$	γ_{opt}
$V_1<V_{1,\mathrm{lim1}}$	$I_{\mathrm{of,opt1}}=0.0058U_{\mathrm{s}}I_{\mathrm{s}}$	$\gamma_{\mathrm{opt1}}=\varphi-2.6033$
$V_1>V_{1,\mathrm{lim2}}$	$I_{\mathrm{of,opt2}}=((5.6043\text{e-}5)V_1-(3.2953\text{e-}4)I_{\mathrm{o,dc}})U_{\mathrm{s}}I_{\mathrm{s}}$	$\gamma_{\mathrm{opt2}}=\varphi-0.5949$
$V_{1,\mathrm{lim1}}\leq V_1\leq V_{2,\mathrm{ref}}$	$\begin{cases} I_{\mathrm{of,opt0}}=0.0029U_{\mathrm{s}}I_{\mathrm{s}} \\ I_{\mathrm{of,opt1}}=0.0058U_{\mathrm{s}}I_{\mathrm{s}} \end{cases}$ $\Rightarrow$ Solve $I_{\mathrm{of,opt3}}$ by (21)	$\begin{cases} \gamma_{\mathrm{opt0}}=\varphi-\arccos(-0.0628I_{\mathrm{o,dc}}) \\ \gamma_{\mathrm{opt1}}=\varphi-2.6033 \end{cases}$ $\Rightarrow$ Solve $I_{\mathrm{of,opt3}}$ by (21)
$V_{2,\mathrm{ref}}\leq V_1\leq V_{1,\mathrm{lim2}}$	$\begin{cases} I_{\mathrm{of,opt0}}=0.0029U_{\mathrm{s}}I_{\mathrm{s}} \\ I_{\mathrm{of,opt2}}\big\|_{V_1=V_{1,\mathrm{lim2}}}=((5.6043\text{e-}5)V_{1,\mathrm{lim2}}-(3.2953\text{e-}4)I_{\mathrm{o,dc}})U_{\mathrm{s}}I_{\mathrm{s}} \end{cases}$ $\Rightarrow$ Solve $I_{\mathrm{of,opt3}}$ by (21)	$\begin{cases} \gamma_{\mathrm{opt0}}=\varphi-\arccos(-0.0628I_{\mathrm{o,dc}}) \\ \gamma_{\mathrm{opt2}}=\varphi-0.5949 \end{cases}$ $\Rightarrow$ Solve $I_{\mathrm{of,opt3}}$ by (21)

An implementation method which is combined with conventional SPS modulation method and SVC method is presented in Fig. 13. G_1 is the PI controller $k_{\mathrm{p}} + k_{\mathrm{i}}/\mathrm{s}$. G_2 is the function relation between δ and i_{o}, i.e., substituting i_{o} with reference value $i_{\mathrm{o,ref}}$ in (8). $i_{\mathrm{o,ref}}$ consists of dc component $I_{\mathrm{odc,ref}}$ and ac fluctuation component $i_{\mathrm{of,ref}}$, i.e., $i_{\mathrm{o,ref}} = I_{\mathrm{odc,ref}} + i_{\mathrm{of,ref}}$. $G_{\mathrm{i}\delta}$ is the power model of DAB as shown in (1). Under this control structure, the output current i_{o} is always equal to its reference value $i_{\mathrm{o,ref}}$.

In order to minimize the current stress and current fluctuations, $i_{\mathrm{of,ref}}$ is supposed to be equal to the optimal value $I_{\mathrm{of,opt}}\cdot\sin(2\omega t + \gamma_{\mathrm{opt}})$. However, $i_{\mathrm{o,ref}}$ is the output of PI controller and $i_{\mathrm{o,ref}}$ cannot be controlled as expected just by tuning the parameters of PI controller. Therefore, a feedforward compensation method is presented to shape the output current i_{o} as expected.

Under steady-state condition, $i_{\mathrm{of,ref}}$ can be derived as (28) according to Fig. 13

$$\begin{aligned} i_{\mathrm{of,ref}} &= -G_1 \cdot v_{2,\mathrm{f}} + i_{\mathrm{f}} \\ &= -V_{2\mathrm{f,opt}}\left(\sqrt{{k_{\mathrm{p}}}^2 + \frac{{k_{\mathrm{i}}}^2}{4\omega^2}}\sin\left(2\omega t + \theta_{\mathrm{opt}} \right.\right. \\ &\qquad\qquad \left.\left. -\ \arctan\left(\frac{k_{\mathrm{i}}}{2\omega k_{\mathrm{p}}}\right)\right)\right) + i_{\mathrm{f}} \\ &\approx -k_{\mathrm{p}} V_{2\mathrm{f,opt}}\sin(2\omega t + \theta_{\mathrm{opt}}) + i_{\mathrm{f}} \end{aligned} \tag{28}$$

$$\begin{aligned} &\text{When } V_1 < V_{1,\mathrm{lim1}} \\ &I_{\mathrm{of,opt5}} = \begin{cases} \frac{\varphi-\varphi_{\mathrm{lim}}}{\frac{\pi}{2}-\varphi_{\mathrm{lim}}}\cdot(I_{\mathrm{of,opt4}} - I_{\mathrm{of,opt1}}) + I_{\mathrm{of,opt1}},\ \varphi_{\mathrm{lim}} < \varphi \leq \frac{\pi}{2} \\ \frac{\varphi+\varphi_{\mathrm{lim}}}{-\frac{\pi}{2}+\varphi_{\mathrm{lim}}}\cdot(I_{\mathrm{of,opt4}} - I_{\mathrm{of,opt1}}) + I_{\mathrm{of,opt1}},\ -\frac{\pi}{2} \leq \varphi < -\varphi_{\mathrm{lim}} \end{cases} \\ &\text{When } V_1 > V_{1,\mathrm{lim2}} \\ &I_{\mathrm{of,opt5}} = \begin{cases} \frac{\varphi-\varphi_{\mathrm{lim}}}{\frac{\pi}{2}-\varphi_{\mathrm{lim}}}\cdot(I_{\mathrm{of,opt4}} - I_{\mathrm{of,opt2}}|_{\varphi=\varphi_{\mathrm{lim}}}) + I_{\mathrm{of,opt2}}|_{\varphi=\varphi_{\mathrm{lim}}},\ \varphi_{\mathrm{lim}} < \varphi \leq \frac{\pi}{2} \\ \frac{\varphi+\varphi_{\mathrm{lim}}}{-\frac{\pi}{2}+\varphi_{\mathrm{lim}}}\cdot(I_{\mathrm{of,opt4}} - I_{\mathrm{of,opt2}}|_{\varphi=-\varphi_{\mathrm{lim}}}) + I_{\mathrm{of,opt2}}|_{\varphi=-\varphi_{\mathrm{lim}}},\ -\frac{\pi}{2} \leq \varphi < -\varphi_{\mathrm{lim}} \end{cases} \\ &\text{When } V_{1,\mathrm{lim}\,1} \leq V_1 \leq V_{1,\mathrm{lim}\,2} \\ &I_{\mathrm{of,opt5}} = \begin{cases} \frac{\varphi-\varphi_{\mathrm{lim}}}{\frac{\pi}{2}-\varphi_{\mathrm{lim}}}\cdot(I_{\mathrm{of,opt4}} - I_{\mathrm{of,opt3}}|_{\varphi=\varphi_{\mathrm{lim}}}) + I_{\mathrm{of,opt3}}|_{\varphi=\varphi_{\mathrm{lim}}},\ \varphi_{\mathrm{lim}} < \varphi \leq \frac{\pi}{2} \\ \frac{\varphi+\varphi_{\mathrm{lim}}}{-\frac{\pi}{2}+\varphi_{\mathrm{lim}}}\cdot(I_{\mathrm{of,opt4}} - I_{\mathrm{of,opt3}}|_{\varphi=-\varphi_{\mathrm{lim}}}) + I_{\mathrm{of,opt3}}|_{\varphi=-\varphi_{\mathrm{lim}}},\ -\frac{\pi}{2} \leq \varphi < -\varphi_{\mathrm{lim}} \end{cases} \end{aligned} \tag{26}$$

$$\begin{aligned} &\text{When } V_1 < V_{1,\mathrm{lim1}} \\ &\gamma_{\mathrm{opt5}} = \begin{cases} -\frac{\varphi-\varphi_{\mathrm{lim}}}{\frac{\pi}{2}-\varphi_{\mathrm{lim}}}\cdot\gamma_{\mathrm{opt1}}|_{\varphi=\varphi_{\mathrm{lim}}} + \gamma_{\mathrm{opt1}}|_{\varphi=\varphi_{\mathrm{lim}}},\ \varphi_{\mathrm{lim}} < \varphi \leq \frac{\pi}{2} \\ -\frac{\varphi+\varphi_{\mathrm{lim}}}{-\frac{\pi}{2}+\varphi_{\mathrm{lim}}}\cdot(\pi + \gamma_{\mathrm{opt1}}|_{\varphi=-\varphi_{\mathrm{lim}}}) + \gamma_{\mathrm{opt1}}|_{\varphi=-\varphi_{\mathrm{lim}}},\ -\frac{\pi}{2} \leq \varphi < -\varphi_{\mathrm{lim}} \end{cases} \\ &\text{When } V_1 > V_{1,\mathrm{lim2}} \\ &\gamma_{\mathrm{opt5}} = \begin{cases} -\frac{\varphi-\varphi_{\mathrm{lim}}}{\frac{\pi}{2}-\varphi_{\mathrm{lim}}}\cdot\gamma_{\mathrm{opt2}}|_{\varphi=\varphi_{\mathrm{lim}}} + \gamma_{\mathrm{opt2}}|_{\varphi=\varphi_{\mathrm{lim}}},\ \varphi_{\mathrm{lim}} < \varphi \leq \frac{\pi}{2} \\ -\frac{\varphi+\varphi_{\mathrm{lim}}}{-\frac{\pi}{2}+\varphi_{\mathrm{lim}}}\cdot(\pi + \gamma_{\mathrm{opt2}}|_{\varphi=-\varphi_{\mathrm{lim}}}) + \gamma_{\mathrm{opt2}}|_{\varphi=-\varphi_{\mathrm{lim}}},\ -\frac{\pi}{2} \leq \varphi < -\varphi_{\mathrm{lim}} \end{cases} \\ &\text{When } V_{1,\mathrm{lim}\,1} \leq V_1 \leq V_{1,\mathrm{lim}\,2} \\ &\gamma_{\mathrm{opt5}} = \begin{cases} -\frac{\varphi-\varphi_{\mathrm{lim}}}{\frac{\pi}{2}-\varphi_{\mathrm{lim}}}\cdot\gamma_{\mathrm{opt3}}|_{\varphi=\varphi_{\mathrm{lim}}} + \gamma_{\mathrm{opt3}}|_{\varphi=\varphi_{\mathrm{lim}}}, \varphi_{\mathrm{lim}} < \varphi \leq \frac{\pi}{2} \\ -\frac{\varphi+\varphi_{\mathrm{lim}}}{-\frac{\pi}{2}+\varphi_{\mathrm{lim}}}\cdot(\pi + \gamma_{\mathrm{opt3}}|_{\varphi=-\varphi_{\mathrm{lim}}}) + \gamma_{\mathrm{opt3}}|_{\varphi=-\varphi_{\mathrm{lim}}},\ -\frac{\pi}{2} \leq \varphi < -\varphi_{\mathrm{lim}} \end{cases} \end{aligned} \tag{27}$$

TABLE V
OPTIMAL VALUES OF $I_{\mathrm{O,F}}$ AND γ WHEN $\varphi < -\varphi_{\mathrm{LIM}}$ OR $\varphi > +\varphi_{\mathrm{LIM}}$

	$I_{\mathrm{of,opt}}$	γ_{opt}
$V_1 < V_{1,\mathrm{lim1}}$	$\begin{cases} I_{\mathrm{of,opt4}} = 0.0031 U_s I_s \\ I_{\mathrm{of,opt1}} = 0.0058 U_s I_s \end{cases}$ $\Rightarrow$ Solve $I_{\mathrm{of,opt5}}$ by (26)	$\gamma_{\mathrm{opt1}}\bigr\rvert_{\varphi=\pm\varphi_{\mathrm{lim}}} = \pm\varphi_{\mathrm{lim}} - 2.6033$ $\Rightarrow$ Solve γ_{opt5} by (27)
$V_1 > V_{1,\mathrm{lim2}}$	$\begin{cases} I_{\mathrm{of,opt4}} = \dfrac{U_s I_s}{100 + (2.182\mathrm{e}6)/V_1^2} \\ I_{\mathrm{of,opt2}}\bigr\rvert_{\varphi=\pm\varphi_{\mathrm{lim}}} \\ = ((5.6043\mathrm{e}\text{-}5)V_1 - (3.2953\mathrm{e}\text{-}4)\, I_{\mathrm{o,dc}}\bigr\rvert_{\varphi=\pm\varphi_{\mathrm{lim}}})U_s I_s \end{cases}$ $\Rightarrow$ Solve $I_{\mathrm{of,opt5}}$ by (26)	$\gamma_{\mathrm{opt2}}\bigr\rvert_{\varphi=\pm\varphi_{\mathrm{lim}}} = \pm\varphi_{\mathrm{lim}} - 0.5949$ $\Rightarrow$ Solve γ_{opt5} by (27)
$V_{1,\mathrm{lim1}} \le V_1 \le V_{2,\mathrm{ref}}$	$\begin{cases} I_{\mathrm{of,opt4}} = 0.0031 U_s I_s \\ I_{\mathrm{of,opt0}} = 0.0029 U_s I_s \\ I_{\mathrm{of,opt1}} = 0.0058 U_s I_s \\ I_{\mathrm{of,opt3}}\bigr\rvert_{\varphi=\pm\varphi_{\mathrm{lim}}} = I_{\mathrm{of,opt1}} + \dfrac{I_{\mathrm{of,opt0}} - I_{\mathrm{of,opt1}}}{V_{2,\mathrm{ref}} - V_{1,\mathrm{lim1}}}(V_1 - V_{1,\mathrm{lim1}}) \end{cases}$ $\Rightarrow$ Solve $I_{\mathrm{of,opt5}}$ by (26)	$\begin{cases} \gamma_{\mathrm{opt0}}\bigr\rvert_{\varphi=\pm\varphi_{\mathrm{lim}}} = \pm\varphi_{\mathrm{lim}} - \arccos(-0.0628\, I_{\mathrm{o,dc}}\bigr\rvert_{\varphi=\pm\varphi_{\mathrm{lim}}}) \\ \gamma_{\mathrm{opt1}}\bigr\rvert_{\varphi=\pm\varphi_{\mathrm{lim}}} = \pm\varphi_{\mathrm{lim}} - 2.6033 \\ \gamma_{\mathrm{opt3}}\bigr\rvert_{\varphi=\pm\varphi_{\mathrm{lim}}} \\ = \gamma_{\mathrm{opt1}}\bigr\rvert_{\varphi=\pm\varphi_{\mathrm{lim}}} + \dfrac{\gamma_{\mathrm{opt0}}\bigr\rvert_{\varphi=\pm\varphi_{\mathrm{lim}}} - \gamma_{\mathrm{opt1}}\bigr\rvert_{\varphi=\pm\varphi_{\mathrm{lim}}}}{V_{2,\mathrm{ref}} - V_{1,\mathrm{lim1}}}(V_1 - V_{1,\mathrm{lim1}}) \end{cases}$ $\Rightarrow$ Solve γ_{opt5} by (27)
$V_{2,\mathrm{ref}} < V_1 \le V_{1,\mathrm{lim2}}$	$\begin{cases} I_{\mathrm{of,opt4}} = \dfrac{U_s I_s}{100 + (2.182\mathrm{e}6)/V_1^2} \\ I_{\mathrm{of,opt0}} = 0.0029 U_s I_s \\ I_{\mathrm{of,opt2}}\bigr\rvert_{\substack{V_1=V_{1,\mathrm{lim2}} \\ \varphi=\pm\varphi_{\mathrm{lim}}}} \\ = ((5.6043\mathrm{e}\text{-}5)V_{1,\mathrm{lim2}} - (3.2953\mathrm{e}\text{-}4)\, I_{\mathrm{o,dc}}\bigr\rvert_{\varphi=\pm\varphi_{\mathrm{lim}}})U_s I_s \\ I_{\mathrm{of,opt3}}\bigr\rvert_{\varphi=\pm\varphi_{\mathrm{lim}}} = I_{\mathrm{of,opt2}}\bigr\rvert_{\substack{V_1=V_{1,\mathrm{lim2}} \\ \varphi=\pm\varphi_{\mathrm{lim}}}} + \\ \dfrac{I_{\mathrm{of,opt0}} - I_{\mathrm{of,opt2}}\bigr\rvert_{\substack{V_1=V_{1,\mathrm{lim2}} \\ \varphi=\pm\varphi_{\mathrm{lim}}}}}{V_{2,\mathrm{ref}} - V_{1,\mathrm{lim2}}}(V_1 - V_{1,\mathrm{lim2}}) \end{cases}$ $\Rightarrow$ Solve $I_{\mathrm{of,opt5}}$ by (26)	$\begin{cases} \gamma_{\mathrm{opt0}}\bigr\rvert_{\varphi=\pm\varphi_{\mathrm{lim}}} = \pm\varphi_{\mathrm{lim}} - \arccos(-0.0628\, I_{\mathrm{o,dc}}\bigr\rvert_{\varphi=\pm\varphi_{\mathrm{lim}}}) \\ \gamma_{\mathrm{opt2}}\bigr\rvert_{\varphi=\pm\varphi_{\mathrm{lim}}} = \pm\varphi_{\mathrm{lim}} - 0.5949 \\ \gamma_{\mathrm{opt3}}\bigr\rvert_{\varphi=\pm\varphi_{\mathrm{lim}}} = \\ \gamma_{\mathrm{opt2}}\bigr\rvert_{\varphi=\pm\varphi_{\mathrm{lim}}} + \dfrac{\gamma_{\mathrm{opt0}}\bigr\rvert_{\varphi=\pm\varphi_{\mathrm{lim}}} - \gamma_{\mathrm{opt2}}\bigr\rvert_{\varphi=\pm\varphi_{\mathrm{lim}}}}{V_{2,\mathrm{ref}} - V_{1,\mathrm{lim2}}}(V_1 - V_{1,\mathrm{lim2}}) \end{cases}$ $\Rightarrow$ Solve γ_{opt5} by (27)

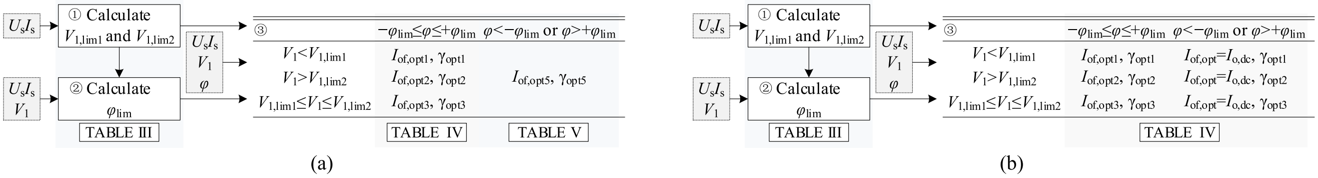

Fig. 12. Online calculation process of $I_{\mathrm{of,opt}}$ and γ_{opt} by (a) SHCS method and (b) simplified SHCS method (SSHCS).

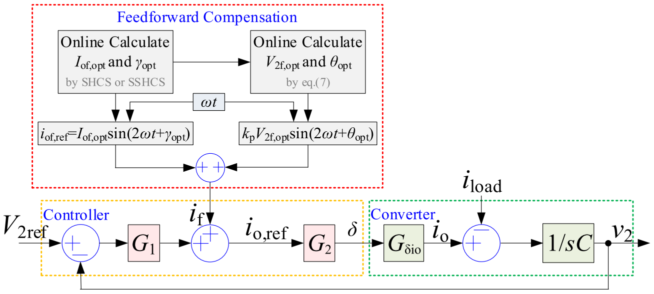

Fig. 13. Control block diagram of SHCS method to suppress current fluctuations.

where $V_{2\mathrm{f,opt}}$ and θ_{opt} are calculated online by (7) when $I_{\mathrm{o,f}} = I_{\mathrm{of,opt}}$ and $\gamma = \gamma_{\mathrm{opt}}$. k_{p} is generally much larger than $k_{\mathrm{i}}/(2\omega)$, so the expression of $i_{\mathrm{of,ref}}$ can be simplified.

Setting $i_{\mathrm{of,ref}} = I_{\mathrm{of,opt}} \cdot \sin(2\omega t + \gamma_{\mathrm{opt}})$, the feedforward current i_{f} can be calculated as follows:

$$i_{\mathrm{f}} = I_{\mathrm{of,opt}}\sin(2\omega t + \gamma_{\mathrm{opt}}) + k_{\mathrm{p}}V_{2\mathrm{f,opt}}\sin(2\omega t + \theta_{\mathrm{opt}}) \tag{29}$$

where ωt is the phase of ac voltage, and $I_{\mathrm{of,opt}}$ and γ_{opt} are calculated online by the method in Fig. 12.

V. PERFORMANCE EVALUATION

A. Deviation Between Nonideal Optimization Effects by SHCS Method and Ideal Optimization Effects by Numerical Method

As can be seen in the derivation process in Sections III and IV, many approximations have been made in the proposed SHCS method to simplify the expressions and to reduce the computation complexity. As a result, the actual optimization effects will deviate from the ideal optimization effects.

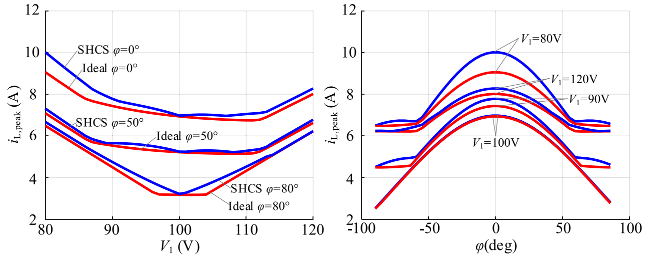

(a) (b)

Fig. 14. $i_{\mathrm{L,peak}}$ varied with V_1 and φ under $V_{2,\mathrm{ref}} = 100$ V, $U_\mathrm{s}I_\mathrm{s} = 400$ VA, and $C = 400$ μF by SHCS method and numerical optimization method. (a) $i_{\mathrm{L,peak}}$ varied with V_1 under different φ. (b) $i_{\mathrm{L,peak}}$ varied with φ under different V_1.

The ideal optimization effects are obtained with the help of numerical method based on (11) and (13) directly. The numerical optimization method will search the optimal points based on the expressions in time domain directly. No approximations have been made to these expressions in time domain. Therefore, the numerical optimization will provide the most accurate optimization results as a reference.

Comparing the optimization results of SHCS method to ideal optimization results, the deviations caused by the approximations and simplifications can be uncovered. As shown in Fig. 14, $i_{\mathrm{L,peak}}$ by SHCS is always higher than ideal results. In the most of the range of V_1, the optimization deviation is very small and can be neglected, as shown in Fig. 14. As φ approaches 0 (unity power factor) and V_1 deviates away from $V_{2,\mathrm{ref}}$, the optimization deviation becomes larger. In fact, the deviation is closely related to the value of capacitance C. When C is designed to be 300, 400, 600, and 800 μF, the maximum relative deviations (when 80 V $\leq V_1 \leq$ 120 V) can be solved as 15%, 11%, 7%, and 5%, respectively. The larger the capacitance C is, the smaller the optimization deviation is.

In most working conditions, the capacitance C is designed to be large enough to avoid affecting normal operation of H-bridge due to the double line-frequency voltage fluctuation on C. If the double line-frequency voltage fluctuation is limited to be smaller than 10% of $V_{2,\mathrm{ref}}$ when the double line-frequency power in (3) is totally absorbed just by capacitance C itself, then C should be designed to be larger than 640 μF in this article and the optimization deviation is smaller than 7% in this case. Moreover, V_1 and V_2 are usually set to match the turn ratio n of high-frequency transformer T, i.e., $V_1 = V_{2,\mathrm{ref}}$ in this article ($n = 1$), to reduce the reactive power in DAB. Therefore, the deviation between V_1 and $V_{2,\mathrm{ref}}$ is not too large. As a result, the optimization effects of SHCS method are as good as the ideal optimization effects in most working conditions.

B. *Comparison of Optimization Effects Between SHCS Method and Traditional Methods*

Some traditional methods try to control the double line-frequency power fluctuations to achieve specific optimization goals as follows:

Method I: This type of method in [19]–[23] is aimed at suppressing the low-frequency fluctuations in input or output current of front-end converter, i.e., $i_{\mathrm{o,f}} = 0$. Equation (10) indicates that the essence of method I is to eliminate the fluctuations in phase-shift ratio δ.

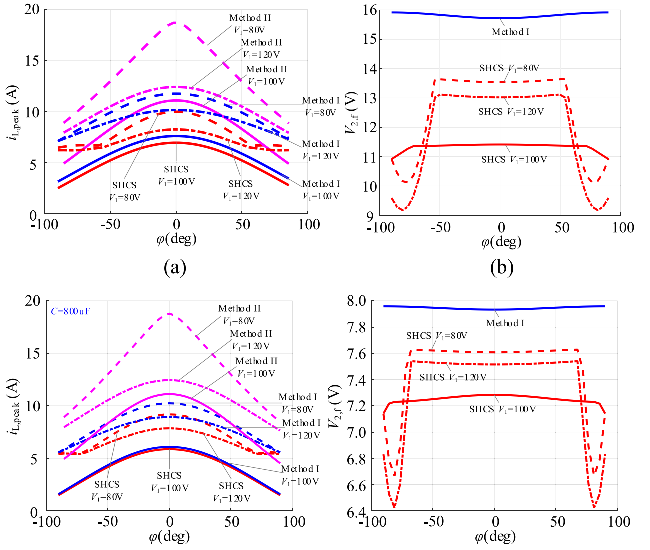

(a) (b)

(c) (d)

Fig. 15. $i_{\mathrm{L,peak}}$ and $V_{2,\mathrm{f}}$ varied with V_1 and φ under $V_{2,\mathrm{ref}} = 100$ V, $U_\mathrm{s}I_\mathrm{s} = 400$ VA by traditional methods and SHCS method. (a) $i_{\mathrm{L,peak}}$ varied with φ under different V_1 when $C = 400$ μF. (b) $V_{2,\mathrm{f}}$ varied with φ under different V_1 when $C = 400$ μF. (c) $i_{\mathrm{L,peak}}$ varied with φ under different V_1 when $C = 800$ μF. (d) $i_{\mathrm{L,peak}}$ varied with φ under different V_1 when $C = 800$ μf.

Method II: This type of method in [12]–[15] is aimed at suppressing the voltage fluctuation of v_2 by providing the low-frequency fluctuating power totally by DAB converter, i.e., $i_{\mathrm{o,f}} = -(U_\mathrm{s}I_s/V_{2,\mathrm{ref}})\cdot\cos(2\omega t + \varphi)$.

The voltage fluctuation amplitude $V_{2,\mathrm{f}}$ in (4) and the current stress $i_{\mathrm{L,peak}}$ in (13) are the two indicators to reveal the optimization effects of traditional methods and SHCS method, as shown in Fig. 15.

Method II eliminates the voltage fluctuation $V_{2,\mathrm{f}}$ at the cost of high current stress $i_{\mathrm{L,peak}}$. In Fig. 15, the $i_{\mathrm{L,peak}}$ by method II is almost two times higher than the $i_{\mathrm{L,peak}}$ by SHCS method. Method II not only increases the power losses of DAB but also increases the risk of devices damage. As a result, method II is not appropriate for DAB to work efficiently and reliably.

Method I can only suppress the low-frequency fluctuations in the propagation path from δ to i_L without considering the high-frequency characteristics of DAB current in (11). According to (11), the low-frequency fluctuations can still propagate from v_2 to i_L. Therefore, the current stress of DAB cannot be reduced to its minimum value, even if $i_{\mathrm{o,f}} = 0$.

Different from method I, the fluctuations in both v_2 and δ have been considered in SHCS method to minimize the current stress of i_L directly rather than i_{in} or i_o. As a result, the $i_{\mathrm{L,peak}}$ by method I is still higher than the $i_{\mathrm{L,peak}}$ by SHCS method, as shown in Fig. 15. Moreover, the practical optimization effects of method I will be poorer than that shown in Fig. 15 if the tradeoff between dynamic performance and reduction of low-frequency fluctuations has to be made [24].

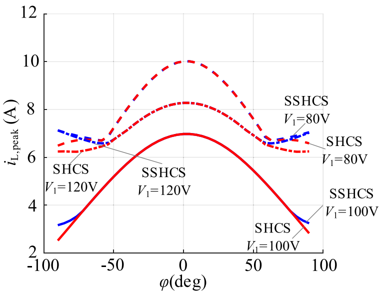

Fig. 16. $i_{\mathrm{L,peak}}$ varied with V_1 and φ under $V_{2,\mathrm{ref}} = 100$ V, $U_\mathrm{s}I_\mathrm{s} = 400$ VA, and $C = 400$ μF by SHCS method and SSHCS method.

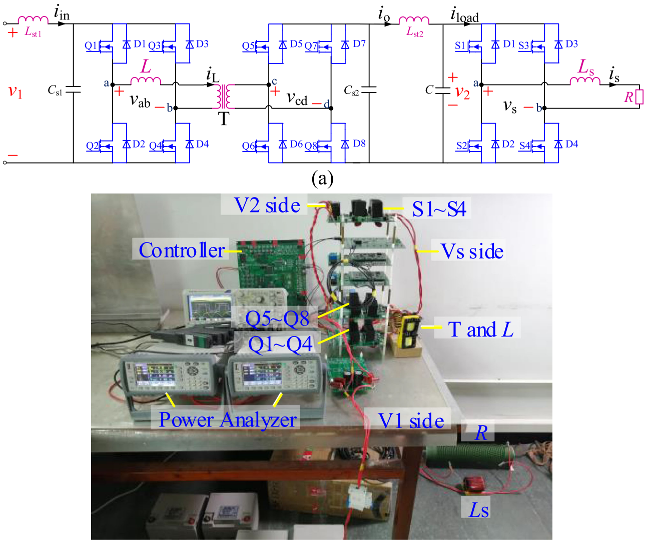

(a)

(b)

Fig. 17. Experimental setup: (a) topology and (b) prototype.

The maximum current stress of DAB occurs in the unity power factor condition. Compared to method II, the $i_{\mathrm{L,peak}}$ of SHCS method decreases by 50%. Compared to method I, the $i_{\mathrm{L,peak}}$ of SHCS method decreases by 20% and the $V_{2,\mathrm{f}}$ of SHCS method decreases by 15%–35%. SHCS method not only has better optimization performance than method I in current stress but also in voltage fluctuations.

As the capacitance C decreases, the deviation of the optimization effects between method I and SHCS method becomes larger, while the optimization effects of method II cannot be affected by C. The advantages of SHCS method become more obvious especially when C is not too large and φ is close to 0.

C. Comparison of Implementation Method Between SHCS Method and Traditional Method I

Method I is the most common method to suppress the low-frequency fluctuations in DAB. There are two common implementation methods:

The first-order low-pass filters are usually used to filter out the double line-frequency fluctuations in closed-loop control system. However, the closed-loop bandwidth has to be cut down to be away from the double line-frequency, resulting in the slow dynamic response of DAB. The tradeoff between filtering effect and dynamic performance has to be made, so that the low-frequency fluctuations in input or output current of DAB cannot be completely filtered out. As a result, the optimization effects of method I are much worse in practice than that shown in Fig. 15.

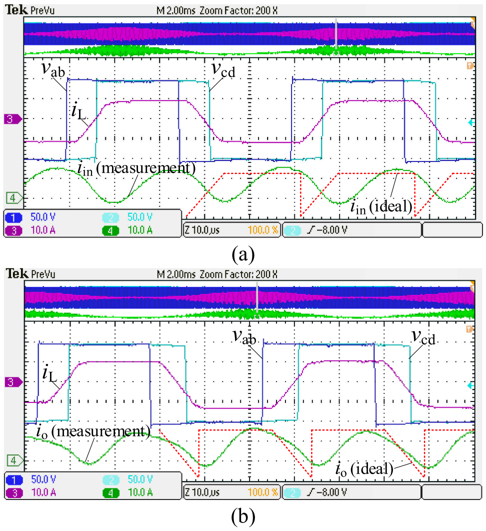

(a)

(b)

Fig. 18. DAB waveforms of v_{ab}, v_{cd}, i_{in}, i_{o}, and i_{L}.

The second-order filters, e.g., band-pass or notch filter, also can be inserted into the closed-loop control system through the feedback paths. Different from the first-order low-pass filters, only double line-frequency components are filtered out by second-order filters. However, large negative phase will be brought into the closed-loop system, leading to a decline in the stability margin of closed-loop system and increasing the design complexity of control parameters.

Different from method I, the proposed SHCS method introduces a feedforward compensation to shape the output current i_o as expected. On the one hand, the feedforward branch only compensates the double line-frequency components, as shown in Fig. 13. Therefore, the feedforward compensation has little impact on the dynamic performance of DAB. No compromises are needed to be made between dynamic response and optimization effects. On the other hand, the feedforward compensation will not affect the stability margin of closed-loop system. Moreover, the control parameters design of SHCS method is the same as that of traditional SVC control. In conclusion, the proposed implementation method of SHCS can overcome the shortcomings of the implementation methods of traditional control methods.

D. Online Computational Burden of Proposed Method

It is worth noting that not all the equations in Tables IV and V have to be calculated online in every control period. The ranges of V_1 and φ will be judged first in every control period to determine which region is feasible in Tables IV or V. The maximum computational burden will occur in the region of Table V when $|\varphi| > \varphi_{\mathrm{lim}}$ and $V_{2,\mathrm{ref}} < V_1 \leq V_{1,\mathrm{lim2}}$. Only five (four) equations are needed to be calculated online for solving

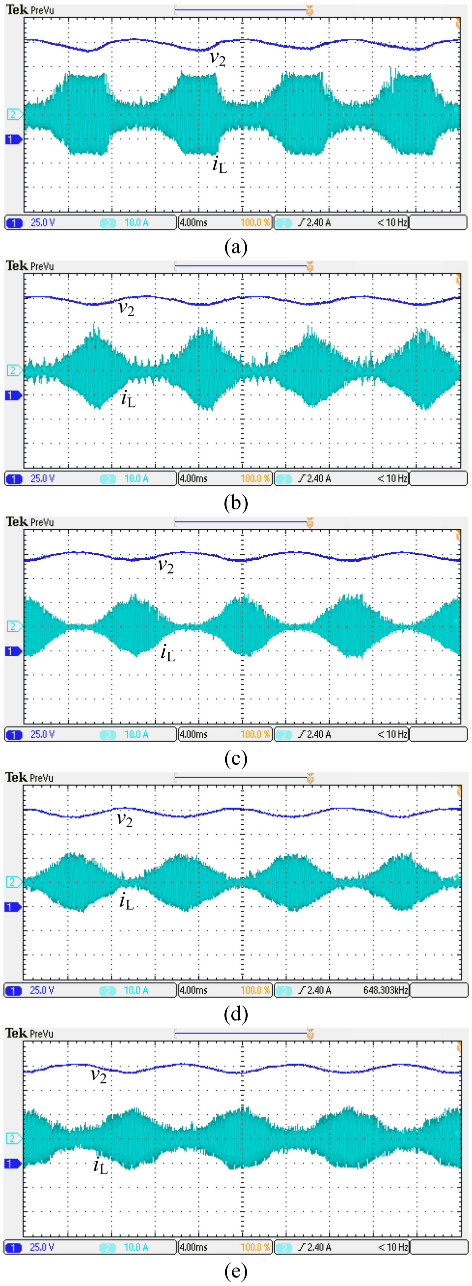

(a)

(b)

(c)

(d)

(e)

Fig. 19. Steady-state waveforms of i_L and v_2 by traditional SVC method when (a) $V_1 = 75$ V, (b) $V_1 = 87$ V, (c) $V_1 = 100$ V, (d) $V_1 = 113$ V, and (e) $V_1 = 123$ V.

$I_{\text{of,opt5}}(\gamma_{\text{opt5}})$. Many approximations and simplifications have been made in these equations. Therefore, the computational burden has been reduced a lot. Compared to multiplication and addition operations, the division operations will occupy much more resources on a digital signal processor. The maximum computational burden can be estimated in Table V that four division operations are needed for solving $I_{\text{of,opt5}}$ and two division operations are needed for solving γ_{opt5}. The maximum computational burden of SHCS method can be acceptable, if the mainstream digital signal processor with floating-point capability is used.

TABLE VI

$V_{\text{2F,OPT}}$, $I_{\text{OF,OPT}}$, γ_{OPT}, AND θ_{OPT} BY SHCS

	V_1=75V	V_1=87V	V_1=100V	V_1=113V	V_1=123V
$V_{\text{2f,opt}}$	13.5	13.2	11.6	12.5	12.4
$I_{\text{of,opt}}$	2.32	2.27	1.15	1.93	2.17
γ_{opt}(rad)	-2.60	-2.57	-1.85	-0.68	-0.6
θ_{opt}(rad)	0.45	0.42	-0.09	-0.6	-0.75

TABLE VII

EXPERIMENTAL RESULTS OF $I_{\text{L,PEAK}}$, $I_{\text{L,RMS}}$, $I_{\text{O,F}}$, $I_{\text{IN,F}}$, AND $V_{\text{2,F}}$ BY SHCS AND SVC

	V_1=75V	V_1=87V	V_1=100V	V_1=113V	V_1=123V
SHCS $i_{\text{L,peak}}$	11A	9A	8A	8A	10A
SVC $i_{\text{L,peak}}$	17A	16A	13A	12A	13A
reduction of $i_{\text{L,peak}}$	35%	45%	39%	33%	23%
SHCS $i_{\text{L,rms}}$	6.5A	5.8A	4.9A	5.2A	5.6A
SVC $i_{\text{L,rms}}$	8.0A	6.9A	5.7A	5.4A	5.7A
reduction of $i^2_{\text{L,rms}}$	34%	29%	24%	8%	3%
SHCS $I_{\text{o,f}}$	2.21A	2.08A	1.19A	2.07A	2.27A
SVC $I_{\text{o,f}}$	3.85A	4.12A	4.13A	4.08A	4.04A
SHCS $I_{\text{in,f}}$	2.40A	1.86A	1.12A	2.28A	2.38A
SVC $I_{\text{in,f}}$	5.29A	4.81A	4.18A	3.56A	3.12A
SHCS $V_{\text{2,f}}$	13.5V	13.2V	11.7V	12.3V	12.8V
SVC $V_{\text{2,f}}$	5.7V	4.2V	3.9V	4.0V	3.7V

In many applications, the converters do not work frequently under the conditions that the power factor is very low. Under this circumstance, the SSHCS method can be used. As a result, the online computational burden can be reduced further. The deviations of optimization effects between SHCS and SSHCS are shown Fig. 16. The maximum deviations (when $\varphi = \pm 90°$) are 14%, 15%, and 6% when $V_1 = 100$, 120, and 80 V, respectively. The deviations are acceptable in the most engineering applications.

VI. EXPERIMENTAL RESULTS

The topology of DAB driving an H-bridge single-phase inverter is shown in Fig. 17. Based on this topology, a small-scale prototype was built to verify the proposed control method. The parameters of the prototype are the same as that in Table II. As can be seen in Figs. 14 and 15, the optimization deviation and current stress reach its maximum value in the worst operating condition when φ is equal to zero, i.e., unity power factor. Therefore, the experimental results under the worst operating condition (unity power factor) are shown as follows.

A. Experimental Results in Steady State

Four capacitors which are placed very close to the four MOSFETs in every full bridge are paralleled to dc-bus (input side and output side), respectively, to absorb the switching spike. These capacitors are shown in Fig. 17(a) as lumped parameters C_{s1} and C_{s2} (4×4.7 μF). However, these wires in PCB circuit and external connections bring about stray inductance L_{st1} and L_{st2} (600 nH). L_{st} and C_s constitute a low-pass filter with cutoff frequency about 50 kHz. As a result, the high-frequency components in i_{in} and i_o are filtered out and the waveforms of i_{in} and i_o are different from that in theoretical, as shown in Fig. 2. In spite of this, the low-frequency components, e.g.,

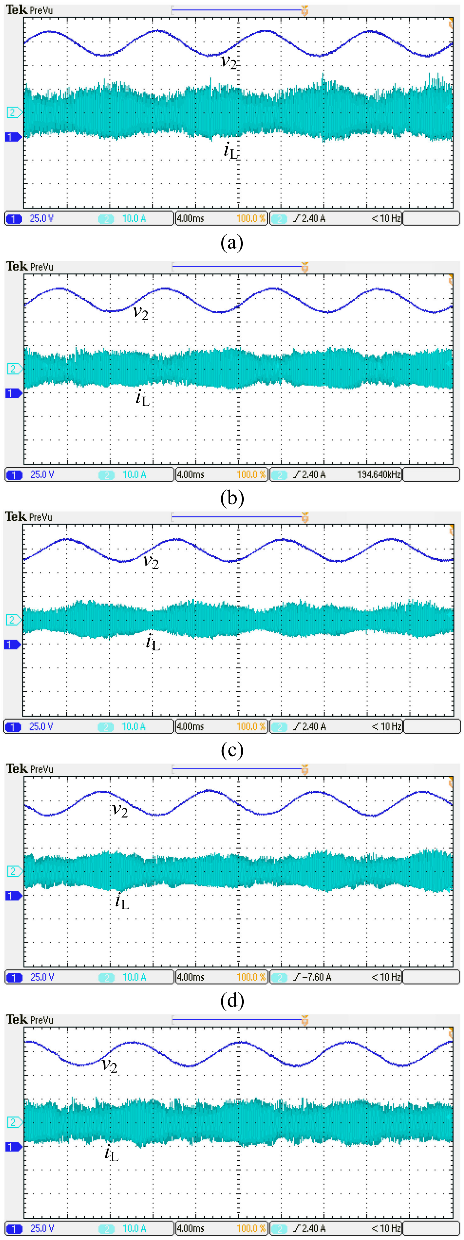

(a)

(b)

(c)

(d)

(e)

Fig. 20. Steady-state waveforms of i_L and v_2 by proposed SHCS method. when (a) V_1=75 V, (b) V_1=87 V, (c) V_1=100 V, (d) V_1=113 V, and (e) V_1=123 V.

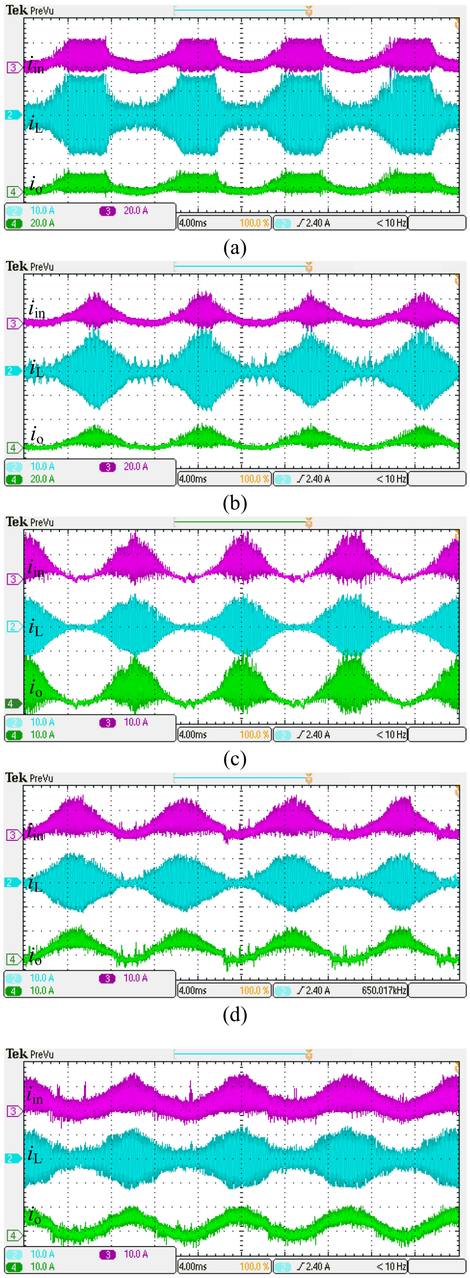

(a)

(b)

(c)

(d)

(e)

Fig. 21. Steady-state waveforms of i_{in}, i_o, and i_L by traditional SVC method when (a) $V_1 = 75$ V, (b) $V_1 = 87$ V, (c) $V_1 = 100$ V, (d) $V_1 = 113$ V, and (e) $V_1 = 123$ V.

the double line-frequency components, still can be extracted from the measured waveforms of i_{in} and i_o without attenuation and distortion (100 Hz $<<$ 50 kHz). The measured and ideal waveforms of i_{in} and i_o are shown in Fig. 18.

The steady-state waveforms of i_L, i_{in}, i_o, and v_2 by SHCS method and traditional SVC method are shown in Fig. 19 based on the parameters in Table II ($U_s{\cdot}I_s = 400$ VA).

The control structure of traditional SVC is the structure in Fig. 13 without the feedforward compensation. By designing the parameters of PI controller, the closed-loop bandwidth of SHCS and SVC are kept the same to be 400 Hz ($k_p = 1, k_i = 10$). $V_{2f,opt}$, $I_{of,opt}$, γ_{opt}, and θ_{opt} are calculated by the equations in Tables IV and V on-chip according to actual operation conditions. The values of $V_{2f,opt}$, $I_{of,opt}$, γ_{opt}, and θ_{opt} under different voltage are shown in Table VI.

According to the experimental results from Figs. 19–22, the current stress and rms value of i_L, the double line-frequency fluctuation of i_{in}, i_o, and v_2 by SHCS and SVC methods are concluded in Table VII as follows.

The proposed SHCS method can significantly suppress the double line-frequency fluctuations in i_L. The current stress of DAB also can be reduced a lot (23%–45%). For example, the current stress has been reduced by 45% when $V_1 = 87$ V.

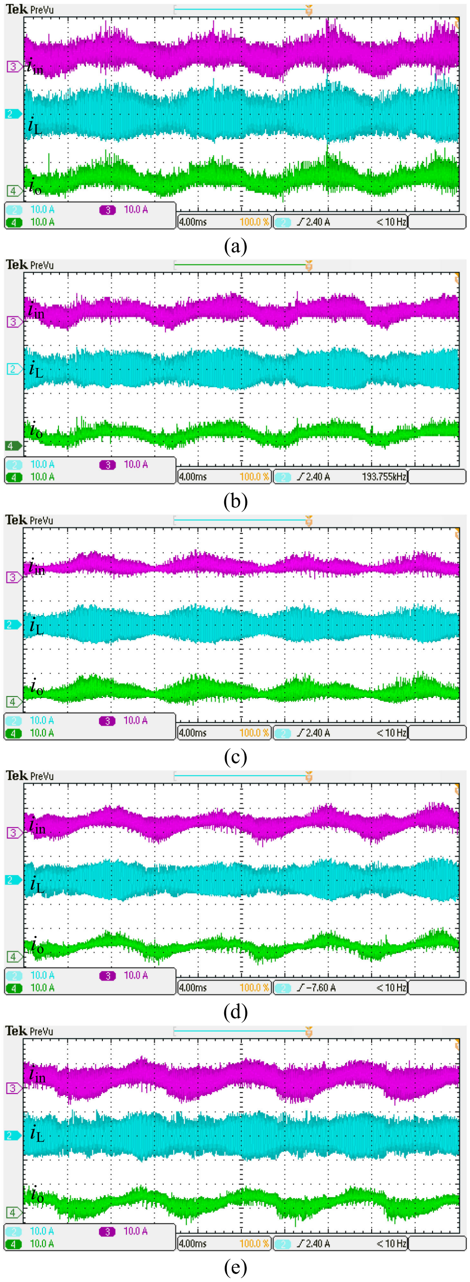

Fig. 22. Steady state waveforms of i_{in}, i_{o}, and i_{L} by proposed SHCS method when (a) $V_1 = 75$ V, (b) $V_1 = 87$ V, (c) $V_1 = 100$ V, (d) $V_1 = 113$ V, and (e) $V_1 = 123$ V.

SHCS method cannot only reduce the current stress, but also reduce the current rms value especially when V_1 is smaller than $V_{2,\mathrm{ref}}$. Although SHCS is not aimed at reducing the rms value of i_{L}, the conduction loss which is almost proportional to $i^2_{\mathrm{L,rms}}$ also can be reduced.

More than that, the double line-frequency fluctuation in i_{in} and i_{o}, i.e., $I_{\mathrm{o,f}}$ and $I_{\mathrm{in,f}}$, are also reduced a lot by SHCS method. The maximum reduction of $I_{\mathrm{o,f}}$ and $I_{\mathrm{in,f}}$ which occurs when $V_1 = 100$ V is about 70%. Although $I_{\mathrm{o,f}}$ and $I_{\mathrm{in,f}}$ have been reduced a lot by SHCS method, they are still obviously larger than 0. It indicates that appropriate double line-frequency fluctuations of input/output current are needed to be injected to dc-bus actively to obtain the best optimal results, instead of simply controlling $I_{\mathrm{o,f}}$ or $I_{\mathrm{in,f}}$ to be 0.

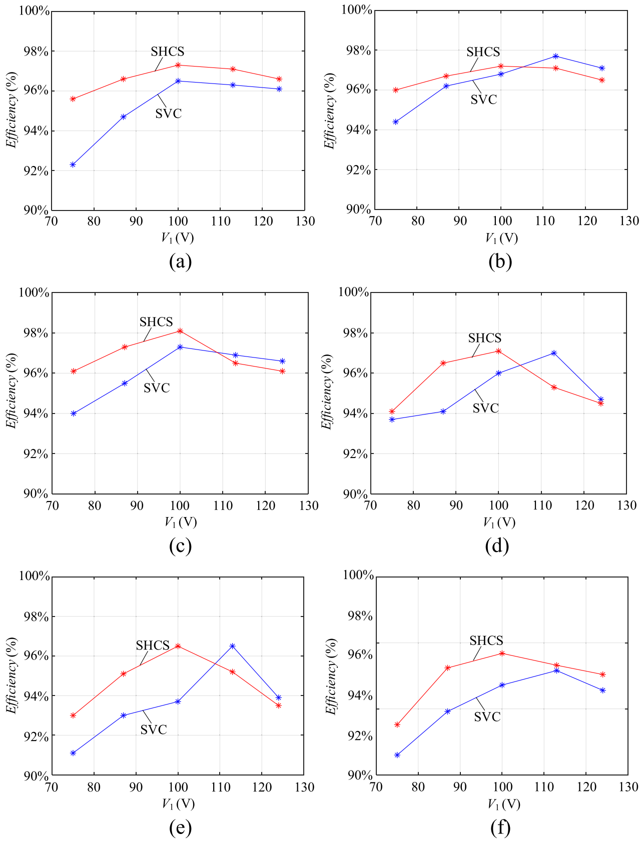

Fig. 23. Efficiency of DAB under single-phase ac load by SVC and SHCS method when (a) 400 W, (b) 320 W, (c) 260 W, (d) 200 W, (e) 140 W, and (f) 80 W.

In conclusion, the experimental results verify the good optimization effects of current stress by SHCS method.

As can be seen in Table VII, the $V_{2,\mathrm{f}}$ by SHCS is larger than the $V_{2,\mathrm{f}}$ by SVC. The reason is explained as follows.

$V_{2,\mathrm{f}}$ and $i_{\mathrm{o,f}}$ by SVC method can be derived as

$$\begin{cases} V_{2,\mathrm{f}} \approx \dfrac{U_{\mathrm{s}} I_{\mathrm{s}}}{\sqrt{(I_{\mathrm{o,dc}} - k_{\mathrm{p}} V_{2,\mathrm{ref}})^2 + 4\omega^2 C^2 V_{2,\mathrm{ref}}^2}} \\ i_{\mathrm{o,f}} \approx V_{2\mathrm{f}} k_{\mathrm{p}} \sin(2\omega t + \theta + \pi) \end{cases} \tag{30}$$

where θ can be calculated by

$$\sin(\theta) = \frac{(V_{2,\mathrm{ref}} k_{\mathrm{p}} - i_{\mathrm{o,dc}}) \cos(\varphi) + 2\omega C V_{2,\mathrm{ref}} \sin(\varphi)}{\sqrt{(V_{2,\mathrm{ref}} k_{\mathrm{p}} - i_{\mathrm{o,dc}})^2 + 4\omega^2 C^2 V_{2,\mathrm{ref}}^2}}$$

$$\cos(\theta) = \frac{(i_{\mathrm{o,dc}} - V_{2,\mathrm{ref}} k_{\mathrm{p}}) \sin(\varphi) + 2\omega C V_{2,\mathrm{ref}} \cos(\varphi)}{\sqrt{(V_{2,\mathrm{ref}} k_{\mathrm{p}} - i_{\mathrm{o,dc}})^2 + 4\omega^2 C^2 V_{2,\mathrm{ref}}^2}}.$$

When $k_{\mathrm{p}} = 1$, the theoretical value of $V_{2,\mathrm{f}}$ is about 4 V. When k_{p} is large enough, $V_{2,\mathrm{f}}$ and θ can be approximated to be $U_{\mathrm{s}} I_{\mathrm{s}}/(k_{\mathrm{p}} V_{2,\mathrm{ref}})$ and $(\varphi + \pi/2)$, respectively, e.g., when $k_{\mathrm{p}} = 1$ (bandwidth is 400 Hz). It indicates that the SVC method tends to method II as k_{p} increases. When k_{p} is small enough, $V_{2,\mathrm{f}}$ and $I_{\mathrm{o,f}}$ can be approximated to be $U_{\mathrm{s}} I_{\mathrm{s}}/(2\omega C V_{2,\mathrm{ref}})$ and 0, respectively, e.g., when $k_{\mathrm{p}} = 0.1$(bandwidth is 40 Hz). It indicates that the

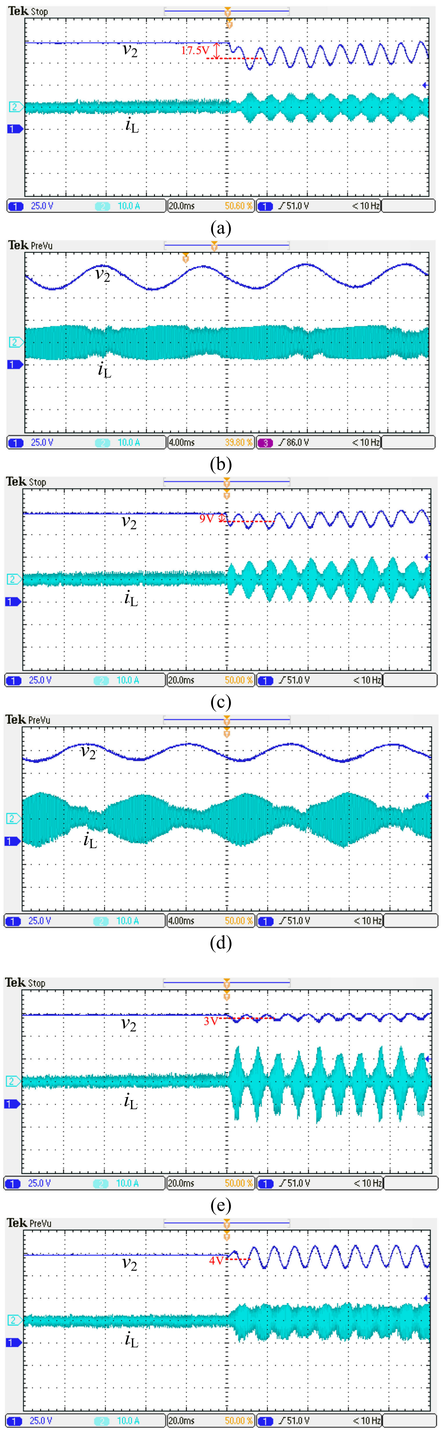

(a) (b) (c) (d) (e) (f)

Fig. 24. Dynamic-state waveforms of i_L and v_2 by traditional method and SHCS method when $V_1 = 85$ V. (a) SVC bandwidth = 40 Hz. (b) Steady-state details of (a). (c) SVC bandwidth = 120 Hz. (d) Steady-state details of (c). (e) SVC bandwidth = 400 Hz. (f) SHCS bandwidth = 400 Hz.

SVC method tends to method I as k_p decreases. As a result, the SVC method in Fig. 19 acts like the method II which can suppress the voltage fluctuation of v_2 effectively. Different from this, the SHCS method is aimed at suppressing the double line-frequency fluctuation of current stress rather than v_2. In fact, as shown in Fig. 15(b), the $V_{2,f}$ by SHCS method($V_{2,f} = 11$–13 V) is larger than the $V_{2,f}$ by method II($V_{2,f} = 0$ V) and is smaller than the $V_{2,f}$ by method I($V_{2,f} = 16$ V).

It is worth noting that the top and bottom of the waveform i_L when $V_1 = 75$ V is flat. This is because the phase-shift ratio δ fluctuates so dramatically that it has been limited to its maximum value 0.5 and cannot increase more. As a result, the actual $V_{2,f}$ is larger than theoretical value 4 V.

The efficiency curves of DAB under varying voltage and load have been given in Fig. 23. SHCS method can obviously improve DAB efficiency especially when V_1 is smaller than V_2. When V_1 is larger than V_2, the reduction of power losses is not obvious. Even under some conditions, the efficiency of SHCS is larger than that of SVC. This is because the conduction losses are the main portion of the power losses of the DAB prototype in this article. The variation tendency of efficiency is almost in accordance with the variation tendency of current rms, as shown in Table VII.

B. Experimental Results in Dynamic State

Inserting a first-order low-pass filter into the SVC control system or reducing the control parameters of PI in SVC is the simplest and the most widely used way to suppress the low-frequency fluctuations in output current of DAB [19], [20]. The essence of this method is to cut down the closed-loop bandwidth, so that the double line-frequency components will be attenuated in the closed-loop paths. However, this method will deteriorate the dynamic performance of DAB. Fig. 24 shows the dynamic state waveforms of i_L and v_2 under step change of load power from zero to nominal value 400 W.

As shown in Fig. 24(a)–(e), when the closed-loop bandwidth is 40, 120, and 400 Hz, the maximum transient voltage dip is 17.5, 9, and 3 V, respectively, while the current stress is 8, 11, and 16 A, respectively. It shows that the low-frequency fluctuations of current increases as the bandwidth increases, while the transient voltage dip decreases as the bandwidth increases. To suppress the low-frequency fluctuations in i_L, the bandwidth 40 Hz is preferable. To suppress the transient voltage dip, the bandwidth 400 Hz is preferable. It indicates that tradeoff between the suppression of current fluctuations and fast dynamic response have to be made. Therefore, the bandwidth 120 Hz may be a better design for SVC method.

As shown in Fig. 24(f), comparing to SVC method with the bandwidth 120 Hz, the current stress is reduced by 27% and the voltage dip is reduced by 55% under SHCS method. It indicates that SHCS method can reduce the current fluctuations significantly without compromise in dynamic performance, just by shaping the double line-frequency fluctuations in the output current of DAB directly.

The second-order filters also can be used [21] but with large negative phase or phase rotation brought into the closed-loop system. It will limit the closed-loop bandwidth, reduce the stability margin, and increase the complexity of parameter design [24]. By contrast, the stability margin and dynamic performance of closed-loop system are not affected by feedforward compensation in SHCS method. Moreover, the design of control parameters in SHCS method is the same as that in traditional SVC method.

The experimental results verify the good performance of SHCS method both in steady state and dynamic state.

VII. CONCLUSION

In this article, the current stress of DAB converter in two-stage single-phase inverter system is minimized by shaping the double line-frequency component in the output current of DAB. The theoretical analysis and experimental results indicate the following conditions.

1) The traditional control methods that are based on the controller design in frequency domain cannot reflect the inherent high-frequency characteristics of DAB current. By contrast, the SHCS method can reduce the current stress of DAB directly based on the analytical expressions in time domain so that both the low-frequency and high-frequency characteristics can be considered. As a result, the current stress can be minimized by SHCS method.
2) The stability and dynamic performance are not affected by the feedforward compensation of only double line-frequency output current. The parameter design of SHCS method is as simple as that of traditional SVC method with just one PI controller. No tradeoff design between dynamic performance and low-frequency fluctuations reduction needs to be made.
3) The feasibility and effectiveness of proposed SHCS method are verified by experimental results. Under high closed-loop bandwidth, the current stress in SHCS method can be reduced by about 30%–50% when compared with traditional SVC method.

REFERENCES

[1] M. A. Hannan *et al.*, "State of the art of solid-state transformers: Advanced topologies, implementation issues, recent progress and improvements," *IEEE Access*, vol. 8, pp. 19113–19132, 2020.

[2] S. Pugliese, M. Andresen, R. A. Mastromauro, G. Buticchi, S. Stasi, and M. Liserre, "A new voltage balancing technique for a three-stage modular smart transformer interfacing a DC multibus," *IEEE Trans. Power Electron.*, vol. 34, no. 3, pp. 2829–2840, Mar. 2019.

[3] A. Iraklis, T. Schirmer, H. Dittus, A. Lusiewicz, and J. Winter, "Overview of three-stage power converter topologies for medium frequency-based railway vehicle traction systems," *IEEE Trans. Veh. Technol.*, vol. 68, no. 4, pp. 3268–3278, Apr. 2019.

[4] S. A. Assadi, H. Matsumoto, M. Moshirvaziri, M. Nasr, M. S. Zaman, and O. Trescases, "Active saturation mitigation in high-density dual-active-bridge DC–DC converter for on-board EV charger applications," *IEEE Trans. Power Electron.*, vol. 35, no. 4, pp. 4376–4387, Apr. 2020.

[5] A. Milczarek and M. Malinowski, "Comparison of classical and smart transformers impact on MV distribution grid," *IEEE Trans. Power Del.*, vol. 35, no. 3, pp. 1339–1347, Jun. 2020.

[6] F. V. Amaral, T. M. Parreiras, G. C. Lobato, A. A. P. Machado, I. A. Pires, and B. de Jesus Cardoso Filho, "Operation of a grid-tied cascaded multilevel converter based on a forward solid-state transformer under unbalanced PV power generation," *IEEE Trans. Ind. Appl.*, vol. 54, no. 5, pp. 5493–5503, Sep./Oct. 2018.

[7] X. Ge and F. Gao, "Flexible third harmonic voltage control of low capacitance cascaded H-bridge STATCOM," *IEEE Power Electron. Lett.*, vol. 33, no. 3, pp. 1884–1889, Mar. 2018.

[8] Y. Hu, X. Zhang, W. Mao, T. Zhao, F. Wang, and Z. Dai, "An optimized third harmonic injection method for reducing DC-link voltage fluctuation and alleviating power imbalance of three-phase cascaded H-bridge photovoltaic inverter," *IEEE Trans. Ind. Electron.*, vol. 67, no. 4, pp. 2488–2498, Apr. 2020.

[9] Y. Hu *et al.*, "High-frequency-link current stress optimization of cascaded H-bridge-based solid-state transformer with third-order harmonic voltage injection," *IEEE J. Emerg. Sel. Topics Power Electron.*, vol. 9, no. 1, pp. 1027–1038, Feb. 2021.

[10] P. Nandi and R. Adda, "Integration of boost-type active power decoupling topology with single-phase switched boost inverter," *IEEE Trans. Ind. Electron.*, vol. 35, no. 11, pp. 11965–11975, Nov. 2020.

[11] D. Neumayr, G. C. Knabben, E. Varescon, D. Bortis, and J. W. Kolar, "Comparative evaluation of a full-and partial-power processing active power buffer for ultra-compact single-phase DC/AC converter systems," *IEEE J. Emerg. Sel. Topics Power Electron.*, vol. 9, no. 2, pp. 1994–2013, Apr. 2021.

[12] H. Qin and J. W. Kimball, "Closed-loop control of DC–DC dual-active-bridge converters driving single-phase inverters," *IEEE Trans. Power Electron.*, vol. 29, no. 2, pp. 1006–1017, Feb. 2014.

[13] F. Xiao, C. Tu, Q. Ge, K. Zhou, Q. Guo, and Z. Lan, "Ripple voltage suppression and control strategy for CHB-based solid-state transformer," *IEEE J. Emerg. Sel. Topics Power Electron.*, vol. 9, no. 1, pp. 1104–1118, Feb. 2021.

[14] T. Isobe, R. A. Barrera-Cardenas, Z. He, Y. Zou, K. Terazono, and H. Tadano, "Control of three-phase solid-state transformer with phase-separated configuration for minimized energy storage capacitors," *IEEE J. Emerg. Sel. Topics Power Electron.*, vol. 8, no. 3, pp. 3014–3028, Sep. 2020.

[15] M. Ali, M. Yaqoob, L. Cao, and K. H. Loo, "Disturbance-observer-based DC-bus voltage control for ripple mitigation and improved dynamic response in two-stage single-phase inverter system," *IEEE Trans. Ind. Electron.*, vol. 66, no. 9, pp. 6836–6845, Sep. 2019.

[16] D. Mou, Q. Luo, J. Li, Y. Wei, and P. Sun, "Five-degree-of-freedom modulation scheme for dual active bridge DC-DC converter," *IEEE Trans. Power Electron.*, vol. 36, no. 9, pp. 10584–10601, Sep. 2021.

[17] J. Sun, L. Qiu, X. Liu, J. Zhang, J. Ma, and Y. Fang, "Optimal simultaneous PWM control for three-phase dual-active-bridge converters to minimize current stress in the whole load range," *IEEE J. Emerg. Sel. Topics Power Electron.*, to be published, doi: 10.1109/JESTPE.2020.3047400.

[18] J. Li, Q. Luo, D. Mou, Y. Wei, P. Sun, and X. Du, "A hybrid five-variable modulation scheme for dual active bridge converter with minimal RMS current," *IEEE Trans. Ind. Electron.*, to be published, doi: 10.1109/TIE.2020.3048278.

[19] M. S. Irfan, A. Ahmed, J. Park, and C. Seo, "Current-sensorless power-decoupling phase-shift dual-half-bridge converter for DC–AC power conversion systems without electrolytic capacitor," *IEEE Trans. Power Electron.*, vol. 32, no. 5, pp. 3610–3622, May 2017.

[20] J. Liu, J. Yang, J. Zhang, Z. Nan, and Q. Zheng, "Voltage balance control based on dual active bridge DC/DC converters in a power electronic traction transformer," *IEEE Trans. Power Electron.*, vol. 33, no. 2, pp. 1696–1714, Feb. 2018.

[21] L. Zhang, X. Ruan, and X. Ren, "Second-harmonic current reduction and dynamic performance improvement in the two-stage inverters: An output impedance perspective," *IEEE Trans. Ind. Electron.*, vol. 62, no. 1, pp. 394–404, Jan. 2015.

[22] D. Wang, B. Nahid-Mobarakeh, and A. Emadi, "Second harmonic current reduction for a battery-driven grid interface with three-phase dual active bridge DC–DC converter," *IEEE Trans. Power Electron.*, vol. 66, no. 11, pp. 9056–9064, Nov. 2019.

[23] L. Zhang, X. Ren, and X. Ruan, "A bandpass filter incorporated into the inductor current feedback path for improving dynamic performance of the front-end DC–DC converter in two-stage inverter," *IEEE Trans. Ind. Electron.*, vol. 61, no. 5, pp. 2316–2325, May 2014.

[24] A. R. Gautam, D. M. Fulwani, R. R. Makineni, A. K. Rathore, and D. Singh, "Control strategies and power decoupling topologies to mitigate 2ω-ripple in single-phase inverters: A review and open challenges," *IEEE Access*, vol. 8, pp. 147533–147559, 2020.

Fei Xiong received the B.S. and Ph.D. degrees in electrical engineering from Beijing Jiaotong University, Beijing, China, in 2013 and 2018, respectively.

He is currently working with the Chongqing University of Posts and Telecommunications, Chongqing, China. His research interests include power electronics technology, energy storage, ac/dc microgrid, and power converter.

Junchi Li was born in Shandong, China, in 1990. He received the B.S. degree from the College of Electrical Engineering, Qingdao University, Qingdao, China, in 2013, and the M.S. degree from the School of Electrical and Electronic Engineering, North China Electric Power University, Beijing, China, in 2016. He is currently working toward the Ph.D. degree in electrical engineering with Beijing Jiaotong University, Beijing, China.

His research interests include power electronic transformer and power electronics for microgrid.

Dong Yan received the B.S. degree from the Harbin University of Science and Technology, Harbin, China, in 2001, and the master's and Ph.D. degrees from the Harbin Institute of Technology, Harbin, China, in 2003 and 2007, respectively.

He is currently working with the Chongqing University of Posts and Telecommunications, Chongqing, China, as a Professor. His research interests include energy router and self-powered source.

Xiaolei Chen received the B.S. degree from the Qingdao University of Science and Technology, Qingdao, China, in 2002, the M.S. degree from the Taiyuan University of Technology, Taiyuan, China, in 2007, and the Ph.D. degree in control science and engineering from Northwestern Polytechnical University, Xi'an, China, in 2016.

He is currently a Lecturer with the School of Automation, Chongqing University of Posts and Telecommunications, Chongqing, China. His research interests include control theory and image processing.